

https://dspace.org/

Robust macroscale superlubricity on carboncoated metallic surfaces

T.K Asumadu; M Vandadi; Desmond Klenam; K Mensah-Darkwa; E Gikunoo ...

https://hdl.handle.net/10539/40497
WOS

Downloaded from a DSpace repository. https://dspace.org/

Applied Materials Today 37 (2024) 102140

Contents lists available at ScienceDirect

Applied Materials Today

journal homepage: www.elsevier.com/locate/apmt

Robust macroscale superlubricity on carbon-coated metallic surfaces

Tabiri Kwayie Asumadu [a,b,c,d], Mobin Vandadi [e], Desmond Edem Primus Klenam [c,f], Kwadwo Mensah-Darkwa [a], Emmanuel Gikunoo [a], Samuel Kwofie [a], Nima Rahbar [c,e,*], Winston Oluwole Soboyejo [c,d,*]

[a] Department of Materials Engineering, Kwame Nkrumah University of Science and Technology, Kumasi, Ghana
[b] Department of Materials Engineering, Sunyani Technical University, Box 206, Sunyani, Ghana
[c] Department of Mechanical Engineering, Worcester Polytechnic Institute, 100 Institute Road, Worcester, MA 01609, USA
[d] State University of New York (SUNY) Polytechnic Institute, College of Engineering, 100 Seymour Road, Utica, NY 13502, USA
[e] Department of Civil Engineering, Worcester Polytechnic Institute, 100 Institute Road, Worcester, MA 01609, USA
[f] Academic Development Unit & School of Chemical and Metallurgical Engineering, University of the Witwatersrand, 1 Jan Smuts Avenue, WITS 2001, Johannesburg, South Africa

ARTICLE INFO

Keywords:
Macroscale superlubricity
Carbon-coatings
Microcontact points
Raman Spectroscopy

ABSTRACT

This paper discusses experimental and computational results of ultralow (near-zero) friction of carbon-coated metallic depositions on substrates of structural steels, Ti, and Ni alloys. The macroscale superlubricity was demonstrated and sustained over several cycles through structurally misoriented carbon coatings on the metallic surfaces. Carbon nanocrystals with variants of graphene footprints were deposited on these metallic surfaces using a novel high temperature biowaste treatment process. The carbon nanocrystals deform, flatten, and coalesce in the wear tracks to form graphitic films leading to a superlubricious coefficient of friction of ~0.003. A coating life of ~150,000 cycles with reduced wear rates was obtained on Ni and steel substrates. The experiments were validated with atomistic simulations providing mechanistic insights into the effects of the graphene variants on the observed frictionless conditions. The underlying mechanisms of the coating/substrate interactions contributing to the macroscale superlubricity are elucidated. The implications of the current results are explored for designing robust and low-cost macroscale superlubricious carbon coatings on metallic substrates. Biowaste is a carbon source within a circular economy that uses material recycling to reduce the global carbon footprint.

1. Introduction

Friction is a ubiquitous phenomenon. Globally, ~100 million terajoules of energy are required to reduce friction, accounting for one-fifth of energy generated annually [1]. About 1 – 4 % of industrialized economies' Gross Domestic Product (GDP) is spent on friction and wear phenomena [2]. About 30 % of the fuel for passenger vehicles is used to overcome friction in the transmission, tires, brakes, and engine [3]. Superlubricity is gaining increasing traction due to the need for reduced energy losses associated with friction and wear phenomena in structural and functional components. Since its inception in the 1980s [4] and 1990s [5], superlubricity has evolved from the nanoscale (attained using graphite coatings in 2004 [6]) to the microscale in 2012 [7]. The transition from the atomistic to the bulk domain is presented in Fig. 1 [8].

Two-dimensional (2D) materials and heterogeneous coatings have been used to achieve superlubricious state [8–16]. The superior lubrication properties of 2D materials, such as carbon-based coatings with varying signatures, contribute to the observed superlubricity mechanism. The sp^2 / sp^3 hybridized configuration and associated carbon networks provide preferable sites for incommensurable surfaces [13,17,18]. Nanostructured carbon rollers also induce superlubricity on metallic substrates [17]. The proposed mechanism that enabled incommensurability was formation of scrolls or nanoscale bearings and passivated materials. This reduces intercalation and tribo-catalyzed (wear interface chemistry modification) surfaces [19]. Reduction in contact areas due to the coated surfaces has been suggested as a driving mechanism.

Four main mechanisms of superlubricity have been elucidated based on the coating-substrate interactions. These are the atomistic interlocking elimination [20], disordered mating interfaces driven by weak van der Waal forces resulting in stick and snap behavior [21], the incommensurability of atomic scale corrugation of surfaces [3,21] and

* Corresponding authors.
E-mail addresses: nrahbar@wpi.edu (N. Rahbar), soboyew@sunypoly.edu (W.O. Soboyejo).

https://doi.org/10.1016/j.apmt.2024.102140
Received 24 October 2023; Received in revised form 5 February 2024; Accepted 21 February 2024
2352-9407/© 2024 Elsevier Ltd. All rights reserved.

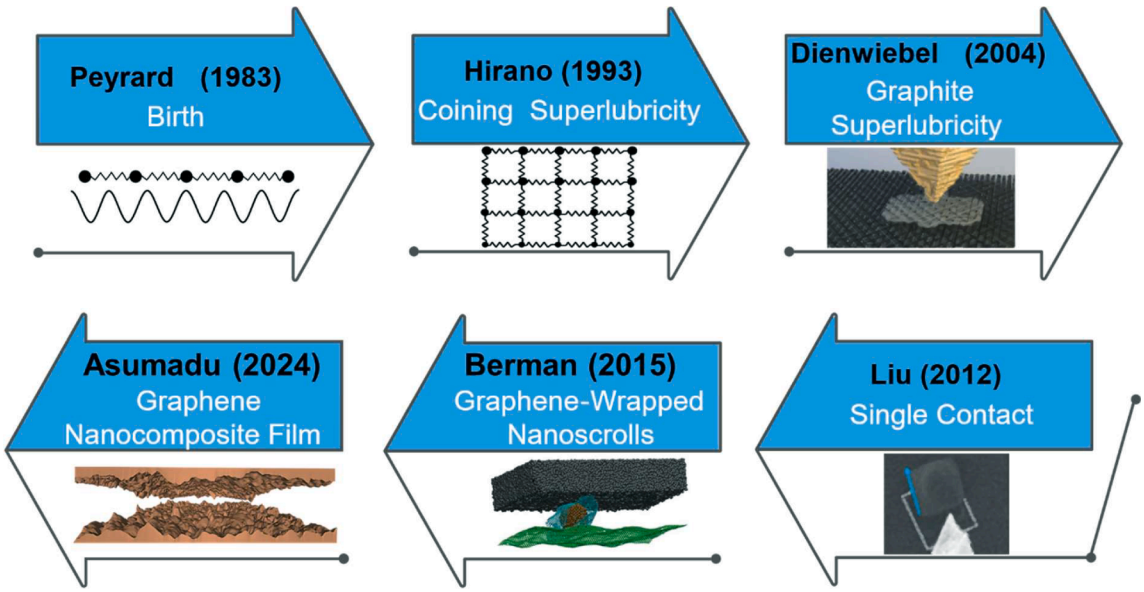

Fig. 1. Timelines for the evolution of superlubricity and the various coating materials applied.

flattening of corrugated surfaces due to significant reduction in potential energy [22]. These reduce the effect of nanoscale asperities on the mating surfaces, leading to substantial decrease in the coefficient of friction, which is low (below 0.001) and sometimes even negative [23–25].

Few studies have demonstrated the concept of macroscale

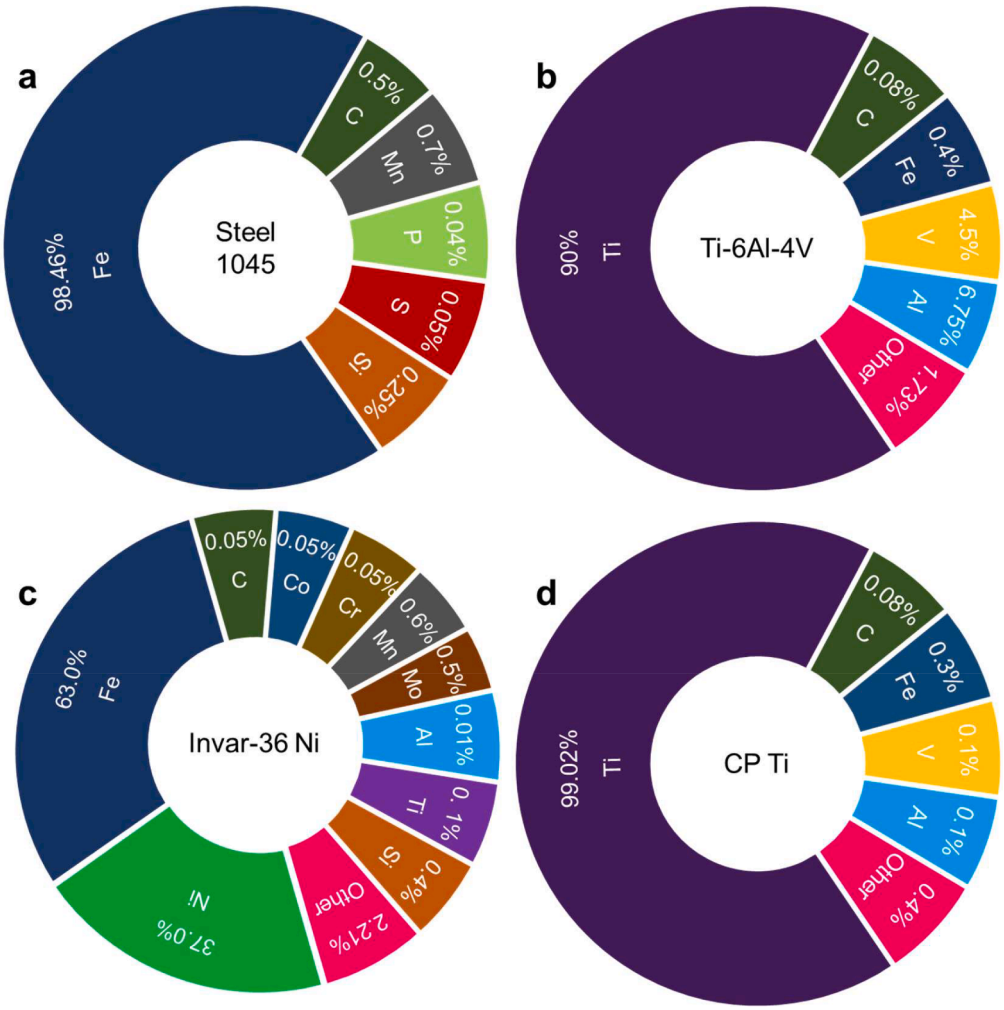

Fig. 2. Average compositions of as-received: (a)1045 Steel, (b) Ti-6Al-4V, (c) Ni-Invar and (d) CP Ti.



Fig. 3. Schematic of the biowaste powder preparation and the carbon nanocrystal deposition during high - temperature biowaste treatment.

superlubricity on metallic substrates [26–29]. Perspectives and reviews have also been carried out [8,10,13,16,30]. However, most superlubricious surfaces were sustained for not more than 5000 cycles, hindering scalability, commercialization, and industrial applications [3]. Therefore, scalability and industrial application hinge on the ability of the coatings to sustain macroscale superlubricity for extended durations (above 40,000) under normal atmospheric conditions. Furthermore, the current deposition techniques used for 2D coatings, such as sputtering and chemical and physical vapor deposition methods, are expensive and not economically viable for large-scale depositions. Current deposition methods' coating morphology, thickness, and topography are unfavorable for macroscale superlubricious contact interactions [31]. These deposition methods are also not situated within the context of a circular economy, decreasing rates of using natural mineral resources, and the need for a low carbon footprint. Therein lies the opportunity for understanding macroscale superlubricity mechanisms and low-cost industrial-scale applications on various metallic substrates without compromising structural integrity.

This work presents a novel bioprocessing method for depositing superlubricious carbon coatings on metallic substrates. The design of the experiment was premised on two fundamental questions. Can carbon nanocrystals and variants of graphene be deposited on bulk metallic substrates by extracting carbon from low-cost biowaste? Can carbon coatings be deposited and oriented structurally to achieve macroscale superlubricity/frictionless conditions for sustained cycles?

Carbon nanocrystals with signatures of graphene variants were deposited on bulk metallic substrates to answer the preceding fundamental questions in superlubricity. The process used a carbon source from "Manihot esculenta" biowaste. This low-cost and sustainable approach fulfills the circular economic model - turning waste into usable raw materials. The technique is simple, easy to design, and less expensive than conventional CVD and PVD techniques currently used for carbon-based coatings. The structural orientation and morphology of the deposited carbon nanocrystals (CNC) and graphene variants lead to robust/sustained macroscale superlubricity on the bulk metallic surfaces for up to 150,000 cycles. A framework for estimating the coating life of mechanical components was devised to provide a mechanistic pathway for coating assessment. The bioprocessing technique significantly reduced the friction coefficient and wear rates on commercially pure (CP) Ti, Ti-6Al-4V, Ni-Invar, and structural steel (AISI 1045) substrates. The implications of the material–manufacturing–mechanisms nexus results are explored for designing of robust and low-cost macroscale superlubricious carbon coatings on metallic substrates.

2. Materials and methods

2.1. Composition of metallic substrates and sample preparation

The substrates used in this work i.e., CP Ti, Ti-6Al-4V, Ni-Invar and AISI 1045 steel were procured from McMaster Carr (Robbinsville, NJ, USA) as rods with a diameter of ~19 mm. Samples with a diameter of ~19 mm and a length of ~10 mm was then fabricated using a Kalamazoo 13AW horizontal bandsaw (Kalamazoo, MI, USA). A water-cooling medium was used to prevent phase transformation during specimen fabrication. Before high-temperature treatment, the specimens were ground with SiC paper (from 100 grits to 1200 grits) using Buehler AutoMet 250 Pro (Lake Bluff, IL, USA), before high temperature treatment. The compositions of the substrates that were used for the deposition are given in Fig. 2.

2.2. Preparation of biowaste as a carbon source

Biowaste, i.e., "Manihot esculenta" leaves, were used as the carbon source. These were dried, milled, and sieved to powder with an average particle size of ~200 µm. The powder was then mixed with $BaCO_3$ in a ratio of 3:1. The $BaCO_3$ was used as an activation compound for the carbon nanocrystal deposition. Fig. 3 is a flow chart of the novel High-Temperature Biowaste Treatment (HTBT) from the processing of the leaves to the deposition layer at 900 °C.

2.3. Carbon nanocrystal deposition using the high temperature biowaste treatment

A metallic crucible (mild steel cylinder) that had an inner diameter of 77.4 mm and an outer diameter of 80.2 mm and a height of 200.3 mm was made for the High-Temperature Biowaste Treatment (HTBT) (Fig. 3). The cylinder was filled with 622 g of processed biowaste powder plus a $BaCO_3$ mixture. Three metallic samples were treated at a time at 900 °C. The 100Cr steel balls and AISI 1045 steel samples were treated for 3 h. The CP Ti, Ti-6Al-4V, Ni-Invar and another batch of AISI 1045 steel samples were treated for 5 h. The cylinder was sealed with high-temperature cement at all exposed joints. The specimens were air-cooled after the treatment. The morphology and deposition stages of the carbon coating were studied within 1 h time intervals.

2.4. Microstructural characterization

Microstructural characterization of the untreated and treated substrates was done with the JEOL JSM – 7000F Field Emission Scanning Electron Microscope (Golden, Co, USA) installed with Electron Backscatter Diffraction (EBSD) and Energy Dispersive Spectroscopy (EDS) systems. The secondary electrons were used to take the microstructural images at 10 kV, a dwell of 5 µs and current of 0.8 nA.

Raman Spectroscopy was used to characterize the carbon nanocrystals on the surfaces of the heat treated substrates, which was also used to characterize the wear tracks within different time intervals. All tests were performed at room temperature (21 °C) with a Horiba XploRa Raman Micro Spectrometer (Kisshoin, Minami-Ku Kyoto, Japan) with 1800-line grating, an aperture of 100, and a slit width of 300. A laser beam with a wavelength of 532 nm and an optical power equivalent to ~10 mW was used to conduct the tests. The Laser light for the test was focused with a 100 x lens on an Olympus microscope integrated with the

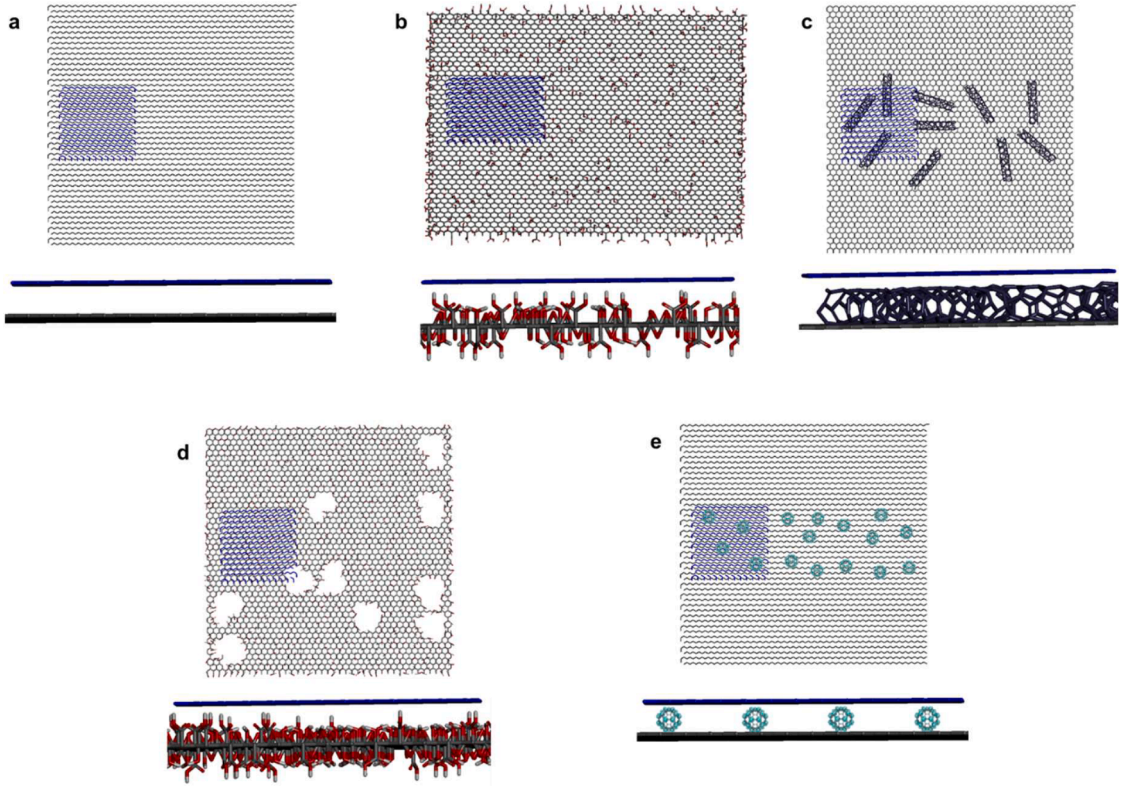

Fig. 4. Schematics of molecular dynamics simulation of the friction surfaces of (a) pristine graphene on pure graphene, (b) pristine graphene on graphene oxide, (c) pristine graphene on carbon nanotubes, (d) pristine graphene on ruptured graphene and (e) pristine graphene on fullerenes.

Horiba XploRa Raman Micro Spectrometer. A silicon wafer (100) was calibrated with a peak of 520 cm^{-1}. The normalization and baseline corrections were done with the LabSpec 6 software provided by Horiba (Kisshoin, Minami-Ku Kyoto, Japan).

The AFM experiments were performed on the surfaces of the substrates after the HTBT treatments using the Park Systems NX20 (Suwon, Korea) setup. The Park System's non-contact PPP-NCHR 10 M cantilevers were used with silicon nitride tips. The nominal radius of the tips was 10 nm, and the tip length of 10 - 15 μm, as reported by the manufacturer. The roughness measurements were conducted in the non-contact mode on the substrates. The recorded images were 1 × 1 μm, 5 × 5 μm, and 25 × 25 μm at a resolution of 1024 × 1024 pixels and a scan rate of 0.17 Hz. The surfaces' root mean square (RMS) roughness was determined as, $R_{RMS} = \sqrt{\frac{1}{n}\sum_{i=1}^{n} z_i^2}$, where z_i is the height at the ith pixel.

X-ray Diffraction (XRD) analysis was conducted to identify the phases present in each structure using a PANalytical Empyrean instrument. Subsequently, Highscore Plus software was used for data interpretation. The XRD measurements were initially taken for the uncoated structure, followed by a post-coating analysis. The comparative results were overlaid to assess the changes introduced by the coating process.

2.5. Friction and wear tests

The ball-on-disk wear tests were carried out with a calibrated Anton Paar TRB^3 tribometer (Peseux, Switzerland) on metallographically prepared untreated and treated substrates. These were performed at loads 1 N, 2 N, and 5 N. Untreated and treated 100Cr steel balls with a 6 mm diameter were used to determine the friction coefficients and wear rates. The tests were conducted without lubrication at room temperature, with a humidity of ~58 %, angular velocities from 100 - 1000 rpm, and an acquisition rate of 10 – 20 Hz. The tests were pulsed at different time intervals to enable the analyses of the wear tracks with Raman spectroscopy, depth characterization, SEM, and EDS. A Taylor Hobson Surtronic S128 Profilometer (Leicester, UK) was also used to characterize the depths of the wear tracks.

The wear rates of the balls were determined by using the worn-out ball height. The worn-out height (h) of the 100Cr steel ball was determined using Eq. (1).

$$h = r - \sqrt{r^2 - \frac{d^2}{4}} \tag{1}$$

where r is the radius of the ball and d is the ball wear scar diameter.

The wear volume of the ball (V_b) was then calculated using Eq. (2). The worn–out volume, V_w, of the as-received and treated samples was also determined using Eq. (3). Finally, the wear rate, k_x, was then calculated using Eq. (4).

$$V_b = \frac{1}{6}\pi h\left(3\frac{d^2}{4} + h^2\right) \tag{2}$$

$$V_w = A_w P d_{max} \tag{3}$$

$$k_x = \frac{V_w}{F \times s} \tag{4}$$

where A_w = worn surface area, Pd_{max} = average penetration depth, F = applied load and s = sliding distance.

The temperature between the counter body and the substrate were measured using a Fluke 62 Max industrial infrared thermometer (Fluke Corporation, Washington, USA). It is single laser targeting device with 10:1 distance to spot ratio. The temperatures were measured in triplicates for each substrate and then averaged. All readings were taken in degree Celsius (°C).

2.6. Molecular dynamics simulations

The Large Atomic/Molecular Parallel Simulator software [32] was used to simulate the nanoscale multiple contact interactions of graphene sheets on different substrates (Fig. 4). The OVITO [33] visualization and analyses software were used to visualize the mating interactions. A time step of 0.1 fs was used for the simulations. The sliding surface was set as a rigid body to omit the deformation caused by the loading and sliding processes. The upper layer of the mating surfaces comprised a single graphene sheet, while the respective mating substrate surfaces consisted of three graphene sheets. The size of the upper graphene layer was 20 $\mathring{A}$ × 20 Å and that for the downward substrates was 100 $\mathring{A}$ × 100 Å. The boundary conditions for the X and Y directions were set to vary periodically, whiles those for the Z directions were fixed. The maximum cut-off radius used was set to half the size of the layers to ensure that the periodic boundary conditions were satisfied and to obtain uniformly distributed stresses in the simulation box (size effect errors were removed). The system was configured to prevent interactions between the mating surfaces before sliding was initiated; It was set to relaxation for the initial step of the simulation.

The conjugate gradient method was used for energy minimization, whiles equilibration was achieved with thermostat and barostat ensembles (each for 1 ns). A downward load of 200 nN was exerted on all the atoms of the moving layer. A consistent interaction was, therefore, obtained between the sliding surfaces. The sliding velocity was set to 10 m/s along the X-axis. The NVE ensemble with a Langevin thermostat was used in the system for the loading and sliding steps. The friction force (f) was calculated as the sum of the forces that act on the substrate along the X-direction. The normal load (N) was also calculated as the sum of forces on the substrate in the Z-direction. The friction coefficient, μ, was then calculated as $\mu = -f/N$.

Two potentials were used in these simulations. The AIREBO potential [34] was used for interactions between carbon atoms in the system. This potential allows covalent bonds to be formed and broken during contact interactions which suits the atomic hybridization in carbon-based systems. The force field used with this potential comprised of three types of interactions, given in Eq. (5).

$$E = \frac{1}{2}\sum_{i}\sum_{j\neq i}\left[E_{ij}^{REBO} + E_{ij}^{LJ} + \sum_{k\neq i,j}\sum_{l\neq i,j,k} E_{kijl}^{TORSION}\right] \tag{5}$$

The REBO (reactive empirical bond-order) potential which calculates reactive interactions between carbon atoms, was also used in the simulations. These interactions are highly coordination dependent. The attraction between the I and J base atoms was adjusted to nearby atoms. Eq. (6) was then used to determine the REBO potential (E_{REBO}).

$$E_{REBO} = \sum_{i}\sum_{j>i}\left[V_R(r_{ij}) + \overline{b_{ij}}V_A(r_{ij})\right], \tag{6}$$

where the term $\overline{b_{ij}}$ is given in Eq. (7)

$$\overline{b_{ij}} = \frac{1}{2}\left(b_{ij} + b_{ji}\right) + \Pi_{ij}^{RC} + b_{ij}^{DH}, \tag{7}$$

and Π_{ij}^{RC} describes radicals and conjugate versus non-conjugate structures. Additionally, b_{ij}^{DH} is the double bond and conjugate bond torsion term, given in Eq. (8).

$$b_{ij} = \left[1 + \sum_{k\neq i,j} f_{ik}(r_{ik})G\left(\cos\theta_{kij}\right)e^{\alpha_{kij}\left[\left(r_{ij}-R_{ij}^{eq}\right)-\left(r_{ik}-R_{ik}^{eq}\right)\right]} + P_{ij}\left(N_i^C, N_i^H\right)\right]^{-\frac{1}{2}} \tag{8}$$

The Lennard-Jones term was used to calculate the longer-ranged interactions. The coefficient for the part of the potential was predefined as $\sigma_{CC} = 3.4_{\mathring{A}}$, and Eq. (9).

$$E_{LJ} = 4\varepsilon\left[\left(\frac{\sigma}{r}\right)^{12} - \left(\frac{\sigma}{r}\right)^{6}\right] \tag{9}$$

A torsion term for 4-body interactions was added to consider dihedral angles. The carbon and oxygen atomic interactions were calculated with Lennard-Jones potential. The dispersion energy and balance distance values were taken from the literature [35].

2.7. Hertzian contact between the surfaces

Hertzian contact theory estimated the stresses and deformation between the two mating surfaces. The contact between the two surfaces depends on the radius of the contact circle, a, indenter load, P, and indenter radius, R. The indentation depth was calculated using Eq. (10), whereas the contact area radius, a, was calculated using Eq. (11).

$$u \approx \left(\frac{2F^2}{E_r^2 R}\right)^{\frac{1}{3}} \tag{10}$$

$$a \approx \left(\frac{3}{2}\frac{RF}{E_r}\right)^{\frac{1}{3}} \tag{11}$$

Where the term E_r is the reduced elastic moduli and was calculated using Eq. (12)

$$\frac{1}{E_r} = \frac{1}{2}\left(\frac{1-v_1^2}{E_1} + \frac{1-v_2^2}{E_2}\right) \tag{12}$$

E_1, v_1, E_2, v_2 are elastic moduli and Poisson ratio of the sphere and plane, respectively. The maximum stress between the sphere and plane was then calculated using Eq. (13).

$$\sigma_{max} = \frac{3}{2}\frac{F}{\pi a^2} = 0.4\left(\frac{E_r^2 F}{R^2}\right)^{\frac{1}{3}} \tag{13}$$

The indenter's contact area and the maximum stress was determined using Eqs. (10) - 13 to be 52 μm and 224 MPa, respectively.

In addition to Hertzian contact theory, we utilized finite element modeling to determine temperature changes during wear testing, employing the ABAQUS software suite for these computations. The dimensions of the ball and substrate were matched to experimental conditions. We engaged an explicit coupled thermal-displacement analysis, starting at an initial system temperature of 300 K. The simulation involved rotating the substrate at 1000 rpm, fixing the ball in the X and Y axes, and applying a 2 N downward force on the ball. Friction at the interface was assumed to convert all frictional energy into heat, with a coefficient of friction aligned with the maximal values obtained experimentally. Moreover, convective heat loss to the ambient air at 295 K was accounted for on all free surfaces. Material properties for the simulation adhered to the specifications [36].

2.8. Hardness test

Micro-indentation measurements were done on the untreated and treated substrates with the Wilson VH3300 hardness tester (Lake Bluff, IL, USA). The Vickers indenter with conical diamond tip was used for the hardness readings. A load of 5 N was applied on the substrates and the indent diagonal lengths were measured with a microscope attached to the hardness tester. The dwell time for all the loads was 10 s, according to the ASTM E2546 – 15 standards. All the Vickers hardness results were then converted to SI units.

3. Results and discussion

3.1. In situ carbon nanocrystal development

A novel High-Temperature Biowaste Treatment (HTBT) method was

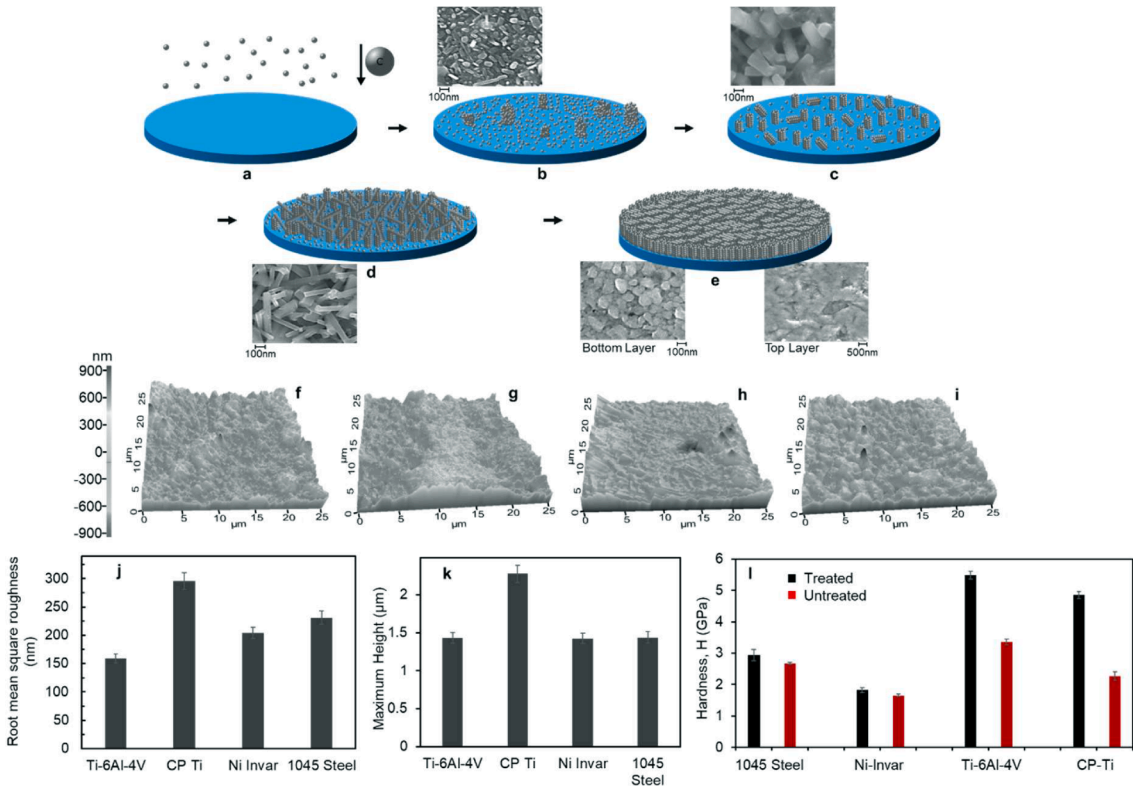

Fig. 5. Stages of deposition of carbon nanocrystal coatings showing: (a) introduction of carbon onto the substrate, (b) crystallization of carbon on the substrate, (c) nanocrystals deposition with vertical and horizontal orientations on the substrate (d) carbon nanocrystals forest on the substrate, (e) fused carbon nanocrystals on substrate with multilayered graphene patches. Non-contact mode AFM showing (f) Ti-6Al-4V, (g) 1045 Steel, (h) Ni Invar and (i) CP Ti. (j) RMS roughness for the surfaces of the treated substrates, and (k) maximum deposited height of carbon nanocrystal coating on substrates, (l) hardness values under treated and untreated conditions.

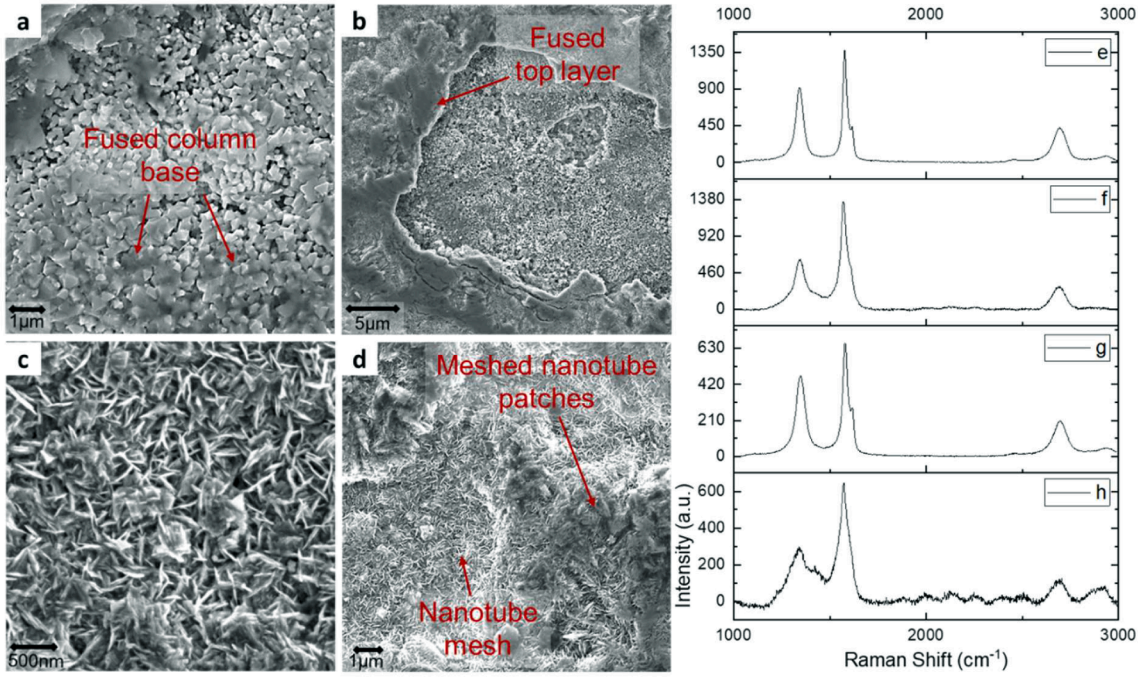

Fig. 6. The SEM images of carbon nanocrystals deposited on Ni-Invar showing: (a) columns of carbon nanocrystal precipitates, (b) fused column layer and the plate-like top coating, (c) high magnification of top carbon nanotube meshed coating and (d) irregular top carbon nanotube meshed coatings with the Raman spectra (e-h) showing graphene signatures.

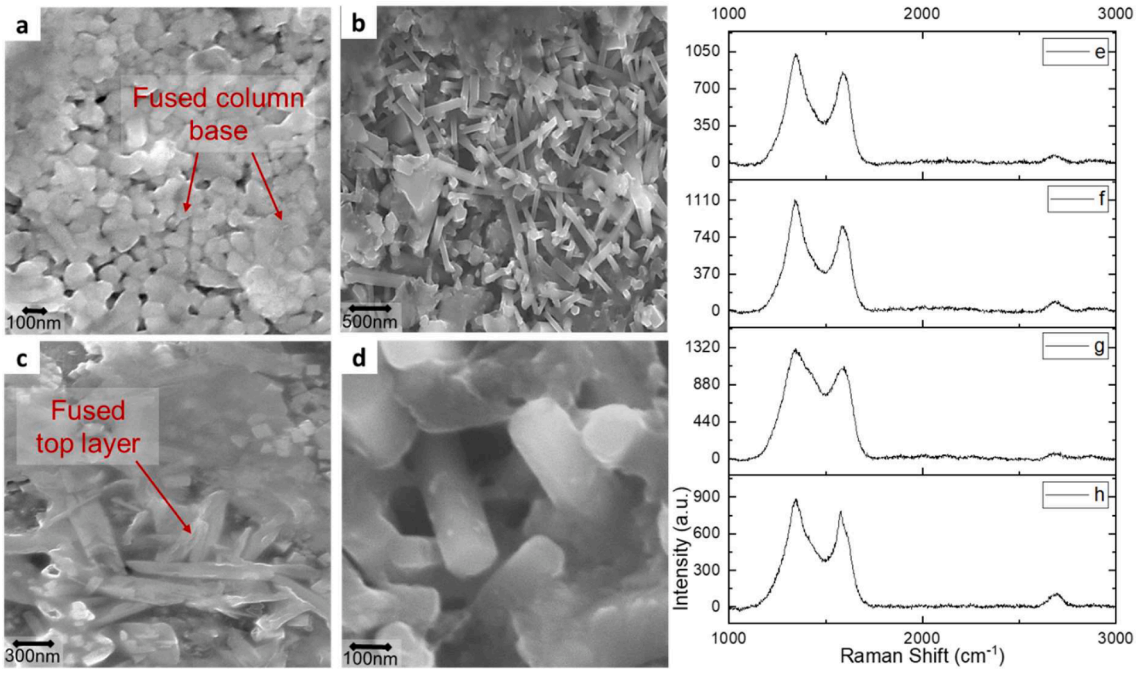

Fig. 7. (a-d) SEM images of Carbon nanocrystals deposited on CP Ti substrates and their Raman spectra (e-h).

used to deposit the carbon nanocrystal coatings. A schematic illustration of the multiple stages of in-situ deposition of the carbon coatings studied within time intervals is shown in Fig. 5. The stages of the in-situ coating deposition started with the diffusion and saturation of carbon into the substrate at 900 °C (Fig. 5(a)). The depth of diffusion and saturation is driven by the solubility of carbon in the substrate [37]. After the surface saturation with carbon, carbon crystals precipitated on the substrate (Fig. 5(b)). The carbon crystals developed into misoriented multiwalled nanotubes, as shown in Fig. 5(c), resulting in the formation of forest-like nanostructures on the substrate (Fig. 5(d)).

The nanocrystals fused at the walls to form a column base for the coating, after which patches of carbon nanocrystals form an upper plate-like layer on it, as shown in Fig. 5(e). The Atomic force microscopy results (Fig. 5 (f - k)) revealed irregular surfaces with multiple micro- and nano-contact points in all the treated substrates. The root mean squared (rms) roughness values obtained for the 1045 steel, Ti-6Al-4V, CP Ti and Ni-Invar were 231.3 nm, 158.9 nm, 295.5 nm, and 204.1 nm, respectively. The respective maximum height of the microcontact points was 1439 nm, 1428 nm, 468.7 nm, and 717.9 nm for 1045 steel, Ti-6Al-4V, CP Ti and Ni Invar. These features, coupled with the misoriented facets of the carbon nanocrystals, are a prerequisite for incommensurability, a condition needed for superlubricious interactions [3,6].

The hardness results of the untreated and treated substrates as shown in Fig. 5(l) reveal an increase in the hardness of the treated substrates.

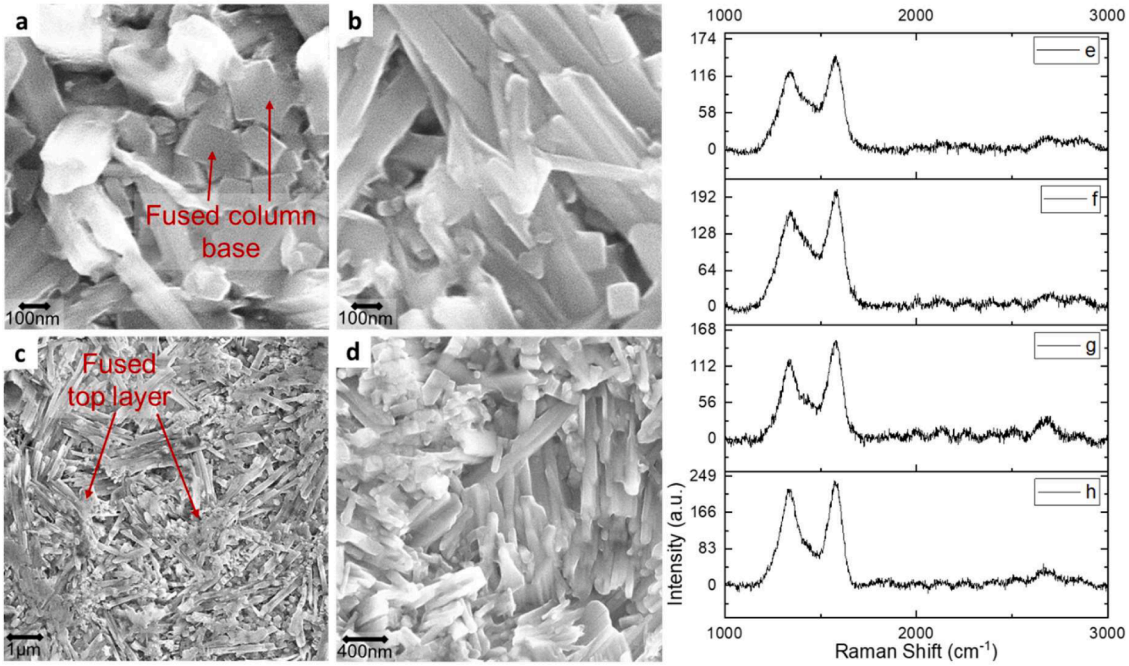

Fig. 8. (a-d): SEM images of carbon nanocrystals deposited on Ti-6Al-4V substrates and their Raman spectra (e-h).

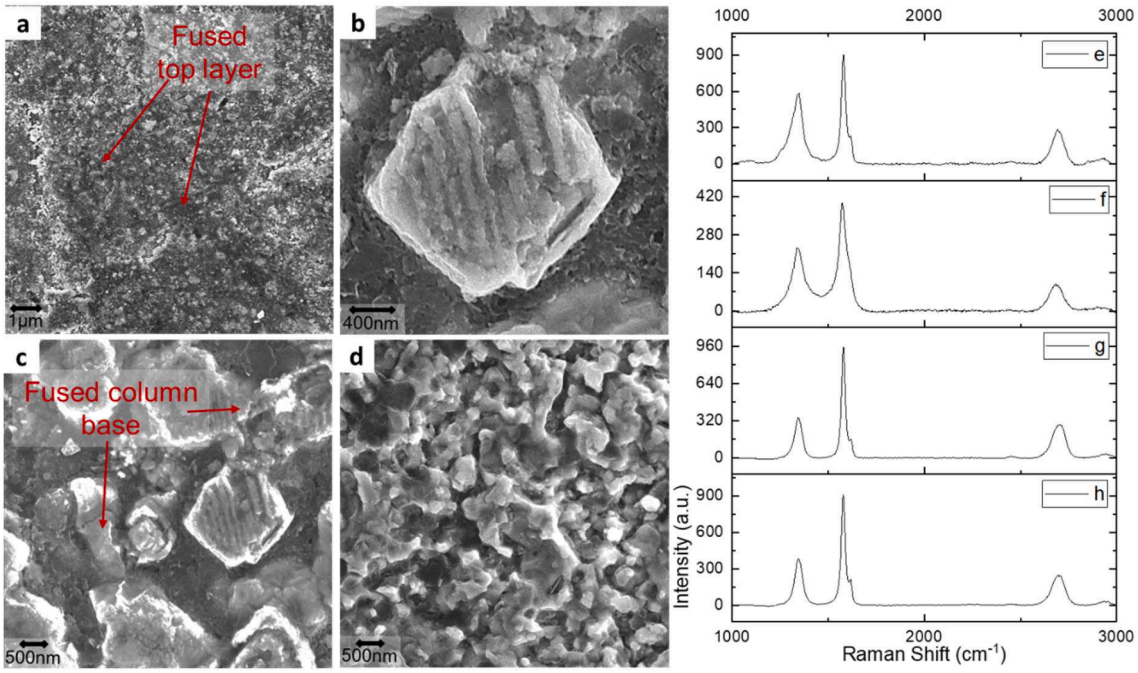

Fig. 9. (a)-(d), SEM images of Carbon nanocrystals deposited on 1045 steel substrates and their Raman spectra (e-h).

The hardness of the untreated 1045 steel, Ni-Invar, Ti-6Al-4V and CP Ti substrates were 2.68 ± 0.028 GPa, 1.66 ± 0.04 GPa, 3.36 ± 0.1 GPa and 2.27 ± 0.14 GPa, respectively. These were increased to 2.93 ± 0.18 GPa, 1.82 ± 0.04 GPa, 5.48 ± 0.12 GPa and 4.85 ± 0.11 GPa for the treated 1045 steel, Ni-Invar, Ti-6Al-4V and CP Ti substrates, respectively. These indicate 9.5 %, 10 %, 63 % and 114 % increase in the hardness of the treated 1045 steel, Ni-Invar, Ti-6Al-4V and CP Ti substrates, respectively. These increase in the hardness of the substrates were attributed to the presence of the carbon coating and diffusion of carbon into the substrates [37–42], which can give rise to a range of dislocation-carbon interactions that increase the overall hardness of the materials [43].

The SEM images of the Ni-Invar substrates with the various Raman spectra are given in Fig. 6. This layer formed ridges and patches that covered most of the substrate surface. Vertically oriented crystals were observed to nucleate from the substrate. These created the base structure of the carbon coating (Fig. 6(a)). The top layer was made up of nanofiber mesh of nano tubes with an average diameter of ~30 ± 12 nm (Fig. 6 (c)). The Raman spectra of the carbon coatings (Fig. 6 (e-h)) had D bands at 1350 cm^{-1}, G bands at 1570 cm^{-1} and 2D bands at 2700 cm^{-1} positions. The intensity ratio I_D/I_G was 0.88 and the I_{2D}/I_G was 0.74. This carbon signature from Raman scatter is associated with defective multilayered and multiwalled graphene platelets and nanotubes [40, 44–49].

The SEM images of the carbon nanocrystals on CP Ti substrates with Raman spectra are shown in Fig. 7. These had misoriented nanocrystals deposited with patches of graphene platelets. The average length of the misoriented nanocrystal structures was ~500 ± 83 nm with an average diameter of ~80 ± 57 nm. The Raman spectra for the carbon nanocrystals on the CP Ti substrates (Fig. 7 (e-h)) had D peaks at 1346 cm^{-1}, G at 1588 cm^{-1} and 2D peaks at 2701 cm^{-1} positions. The intensity ratio for I_D/I_G was 1.1 and that for I_{2D}/I_G was 0.69. This intensity is synonymous with Raman signature for multiwalled carbon nanotubes [44,46, 50]. The disorder in D and G peaks can be attributed to the Ti-doping of the graphene structure [51].

The SEM images and Raman spectra obtained for the carbon nanocrystals deposited on the Ti-6Al-4V substrates are given in Fig. 8. The SEM images show randomly oriented carbon nanocrystals on the surface of the substrates. The Raman spectra (Fig. 8 (e – h)) had D bands at 1346 cm^{-1}, G bands at 1578 cm^{-1} and 2D bands at 2665 cm^{-1} positions. The I_D/I_G ratio was 1.0 and that of I_{2D}/I_G was also 0.84 which are Raman signatures linked to Ti and Al-doped multiwalled carbon nanocrystals [51].

The SEM images and Raman spectra of the carbon nanocrystal coating on the 1045 steel substrates are presented in Fig. 9. These reveal vertical carbon nanocrystals, sintered graphene plates and multiwalled nanotubes on the substrates. The Raman spectra (Fig. 9 (e - h)) for this coating had a D band for at 1346 cm^{-1}, a G band for 1577 cm^{-1} and a 2D band for 2695 cm^{-1}, respectively. The I_D/I_G intensity ratio was 0.74 and that for I_{2D}/I_G was 0.68. These ratios were associated with defective multilayered/multiwalled graphene deposits [40,44–49].

3.2. *Superlubricity and coefficient of friction evolution*

The Friction coefficient plots obtained from the untreated and treated metallic substrates are presented in Fig. 10. Typical topographic images of the mating surfaces obtained using non-contact mode AFM are demonstrated in Fig. 10(a). These are incommensurable surfaces with apparent multiple nano- and microcontact points. Fig. 10(c) shows ultra-low friction results for the sliding test on the treated 1045 steel and Ni-Invar substrates. The three main transition zones of friction coefficients and associated microstructural characterization of the graphitic coating are given in Fig. 10(c (i - iii)). The initial state was associated with low friction coefficients from 0 to ~1000 cycles before a transition to ultra-low CoF values up to ~0.003 and ~0.01 (for cycles above 1000 for the treated Ni-Invar and 1045 steel substrates (Fig. 10(c)). The initial low CoF phase was associated with preliminary multiple microcontact interactions between the walls of the carbon nanocrystals on the contacting surfaces. The SEM image of the carbon nanocrystals on the wear tracks is presented in Fig. 10(c (i)). The irregularly deformed surfaces reveal evidence of flattening carbon nanocrystals with a range of orientations.

Continuous load bearing and sliding action led to the deformation, coalescence, and fusion of carbon nanocrystals into graphene composite flakes (Fig. 10 (c (ii))). These flakes subsequently coalesced into graphene nanocomposite films (GNCF) that intercalated between the treated 100Cr steel ball and the treated substrates, as shown in Fig. 10 (c (iii)). The corrugated graphitic films (on the ball and substrate) separating the contacting surfaces at the micron and submicron scales (as

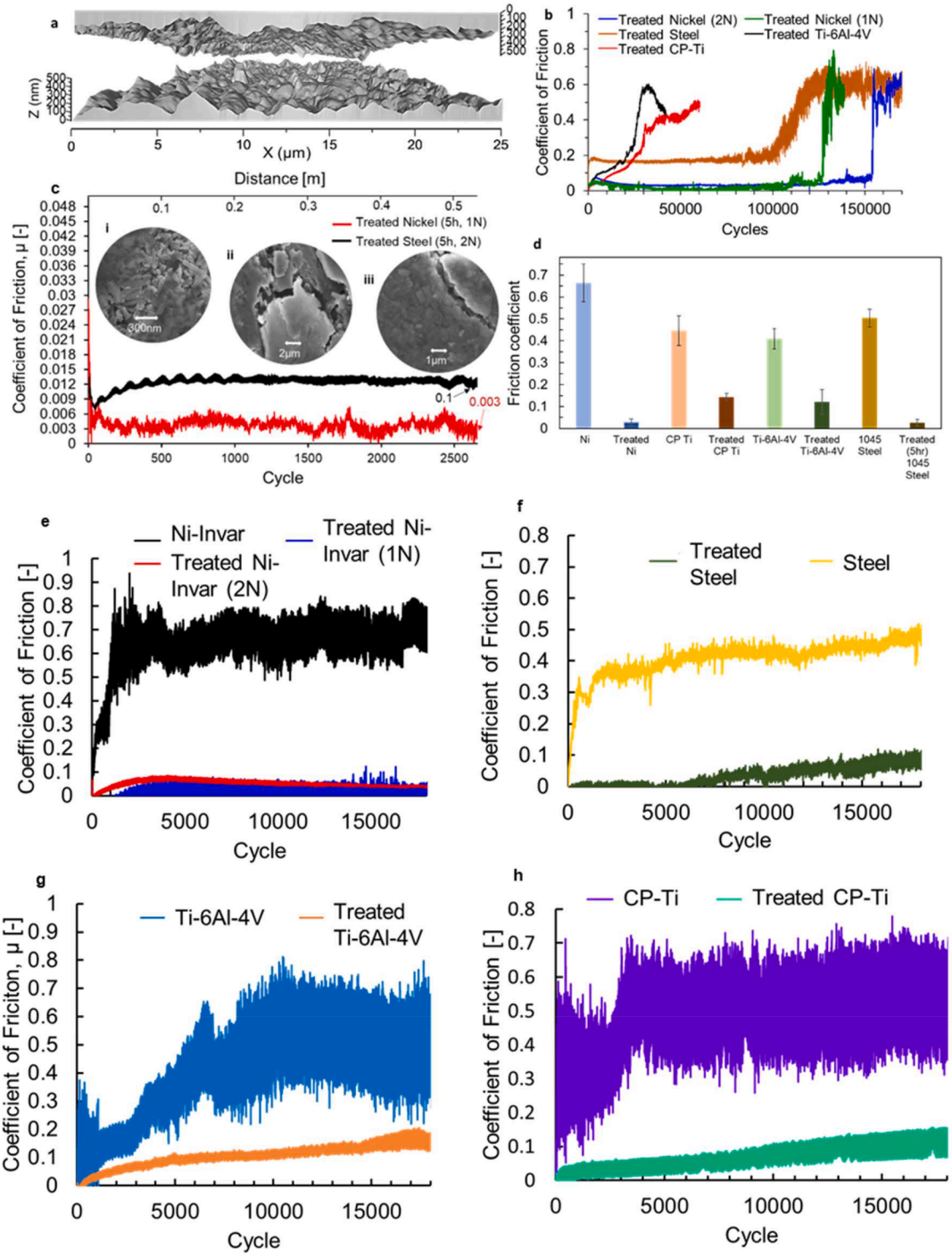

Fig. 10. AFM, SEM and friction results showing (a) non-contact mode AFM topographical results of mating surfaces showing incommensurable multiple nano- and microcontact points, (b) Coefficient of Friction versus the number of cycles plot of treated 1045 steel (treated for 5 h at 900 °C, 2 N load and 1000 rpm) and treated Ni-Invar (treated for 5 h at 900 °C, 1 N load and 1000 rpm), and (i-iii), their underlying SEM images at various stages of carbon nanocrystal deformation; (c) CoF evolution curves for the treated Ni-Invar (treated for 5 h at 900 °C, 1&2 N load, 1000 rpm), 1045 steel (treated for 3 h at 900 °C, 2 N load, 1000 rpm), CP Ti (treated for 5 h at 900 °C, 2 N load, 1000 rpm) and Ti-6Al-4V (treated for 5 h at 900 °C, 2 N load, 1000 rpm) substrates, (d) Friction coefficients for the treated and untreated metallic substrates. Coefficient of Friction versus number of cycles plots in the stabilized regimes of treated substrates (tests done with treated 100Cr Steel ball), as compared to untreated substrates (done with untreated 100Cr Steel ball) of (e) Ni-Invar, (f) Ti-6Al-4V (g) 1045 stee and (h) CP Ti.

shown in Fig. 17(i)-(l)) provide the conditions required for sustained macroscale superlubricity [3]. The ultra-low friction regimes are associated with the flattening of corrugated surfaces as shown in Fig. 10(c)(i-iii)) and Fig. 17 (i-j), which results in decreasing friction force as the normal force increases [3,22,52]. The root mean square roughness values of the nano- and microcontact points on the 1000 cycles wear tracks of the treated Ti-6Al-4V, CP Ti, Ni-Invar and 1045 steel were 65 ± 8.03 nm, 129.59 ± 27.31 nm, 122.1 ± 34.22 nm and 128.6 ± 40.12 nm, respectively. These roughness values were lower than those observed before the wear tests were conducted, due to the flattening and formation of the graphene nanocomposite films in the wear tracks.

The evolution of CoFs for the treated substrates is shown in Fig. 10 (b). The CoFs increased from plunging states at the beginning of the test to stable mean values. On average, these were sustained for several

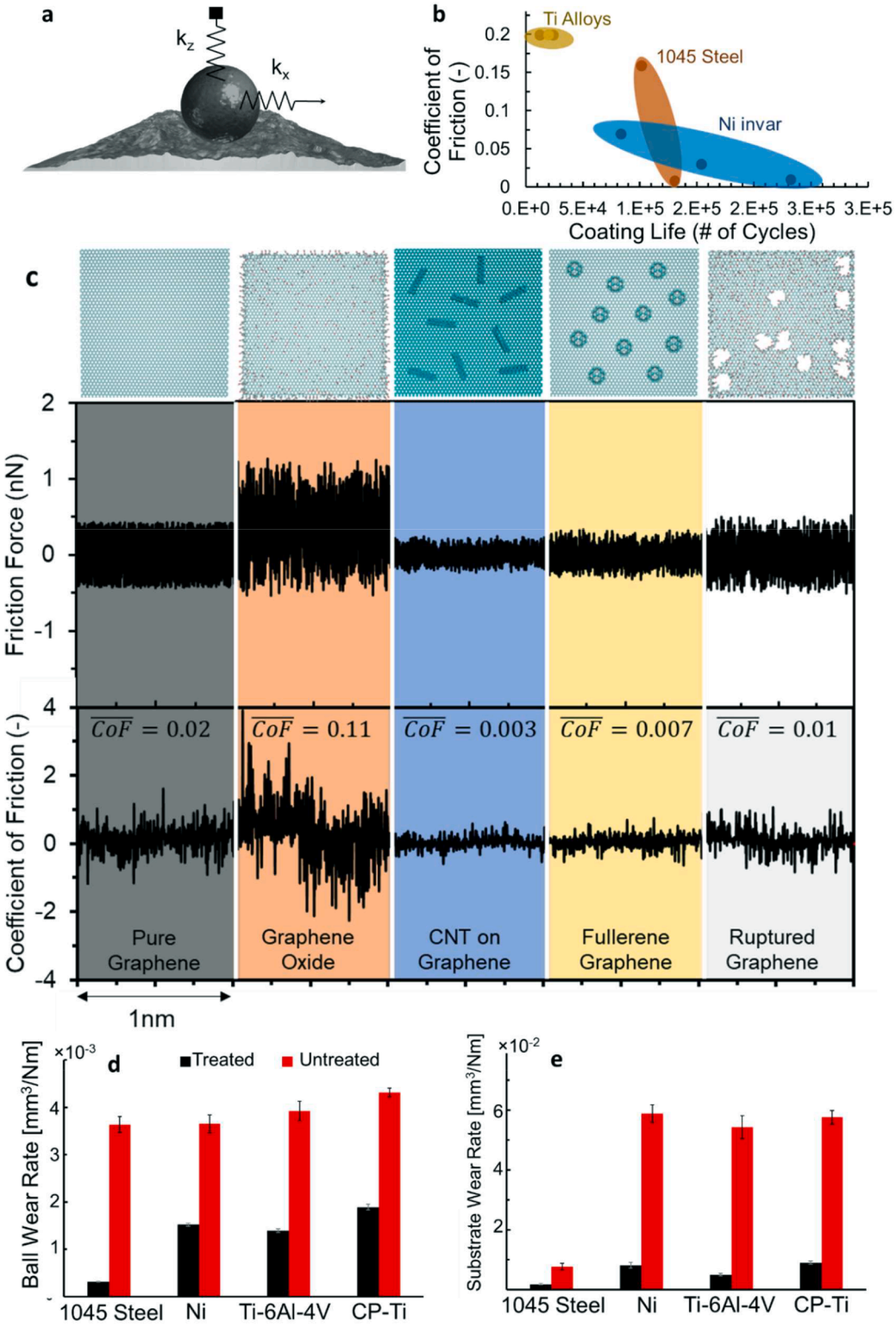

Fig. 11. Mechanistic simulations and wear life of coatings showing (a) schematic of the ball on disk setup for MD simulation, (b) coefficient of friction and the coating life merit index of Ni-Invar, 1045 steel, and Ti alloys, showing the range for the graphitic protection on the substrates. (c) coefficient of friction and friction force simulations schematic and results for graphene on pure graphene, graphene oxide, carbon nanotubes, fullerene, and raptured graphene surfaces (d) wear rate of the treated and untreated balls used as counter body, (e) wear rate of treated and untreated substrates.

cycles (depending on the material) before transitioning to high friction coefficients. These trends indicate of a change in the friction mechanisms and the end of the graphitic protection. After the initial plunging, the CoF for the treated Ni-Invar at 1 N load was stabilized at a mean value of ~0.007 and maintained for ~120,000 number of cycles to failure with a corresponding CoF of 0.5. However, at 2 N, the mean stabilized CoF was at ~0.027 and was sustained for ~150,000 cycles to failure before transitioning to a mean CoF of 0.58. For the 5 N load at 500 rpm, a high CoF of 0.29 on average was observed in the stabilized regime. The corresponding number of cycles to failure sustained was

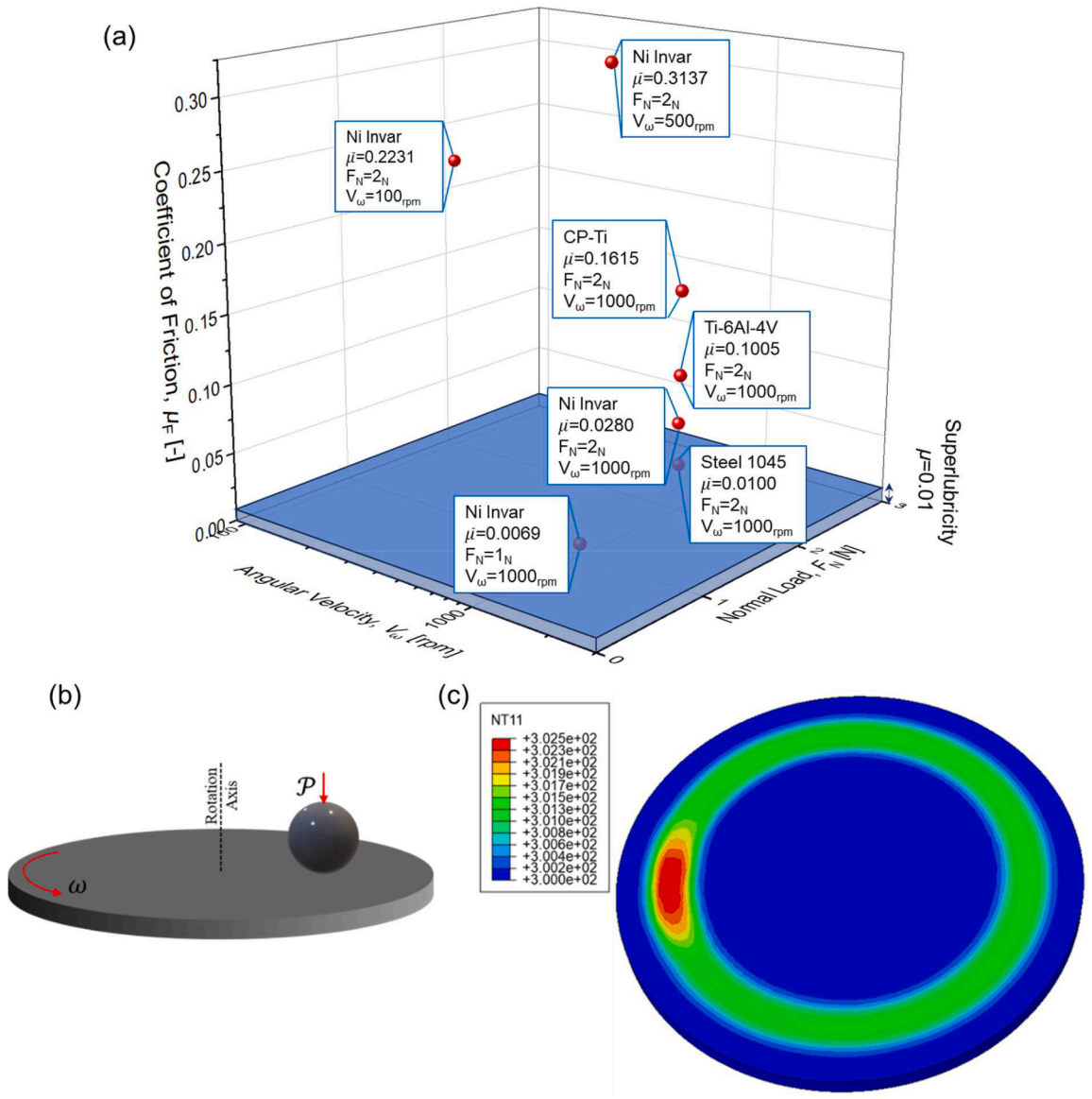

Fig. 12. (a) Summary of conditions for friction experiments indicating the preconditions for the superlubricity regime with substrates treated for 5 h, (b) schematics showing the finite element model (c) finite element analysis based on the dissipation of heat between the mating surfaces.

~70,000 cycles before transitioning to a higher CoF value. The stabilized CoF obtained for the treated 1045 steel (treated for 3 hrs) was 0.15 on average. This value was sustained for ~100,000 cycles, with an average final transitioned CoF value of 0.6.

The CoF of the treated Ti-based alloys showed a similar trend to the Ni and 1045 steel alloys. The CP – Ti alloys were stabilized at ~0.12 with corresponding number of cycles to failure being ~18,000 and transitioned at CoF of 0.58 on average. For the treated Ti – 6Al – 4 V, the stabilized CoF was ~0.098 and sustained for ~20,000 cycles. After the deterioration of the carbon coatings, there was a transition from the low CoF to a high value of 0.57 on average. The extent of CoF reduction for the treated and untreated substrates in the stabilized regime is shown in Fig. 10 (e-h). The reduction of the CoF of the treated metallic substrates was on average 95.8 % for Ni Invar, 94.8 %, for 1045 steel, 70.7 % for Ti-6Al-4V and 68.9 % for CP – Ti (Fig. 10(d)). This overall reduction is due to the graphitic protection that enhanced carbon-carbon interactions on the coated surfaces. Although, the CoF and the number of cycles to failure of the carbon-coated CP – Ti substrate was lowest, it was higher than data for some alloys published [17,53]. The number of cycles to failure is enough to ensure that catastrophic failures are prohibited for most standard applications with less aggressive abrasive and adhesive wear. The extended number of cycles to failure on the Ni – Invar and the steel alloys would also lead to a prolonged lifecycle for materials used in high friction and wear applications.

Nano- and micro-scale superlubricity have been observed on graphitic [6] and heterogeneous surfaces [54], whereas centimetres-long superlubricity has been observed in double-walled carbon nanotube experiments [55]. However, the challenge with these experiments is the limited contact interactions between the mating surfaces, which could not induce sustained macroscale superlubricity. Large-scale nano- and microcontacts interactions (as shown in Fig. 17 (i-l) are needed to achieve sustained macroscale superlubricity, with high proportions of the nano- and microcontacts under a superlubricious state [6,17]. Thus, a minority of microcontacts will therefore be in the registry, preventing full commensurability.

In our work, the GNCF induced large-scale nano and microcontact points on the substrate and the counter body (100Cr ball), contributing to the observed macroscale superlubricity with sustained coating life. Corrugated and incommensurable graphene nanocomposite films between the contacting surfaces also enable this effect. Within the GNCF

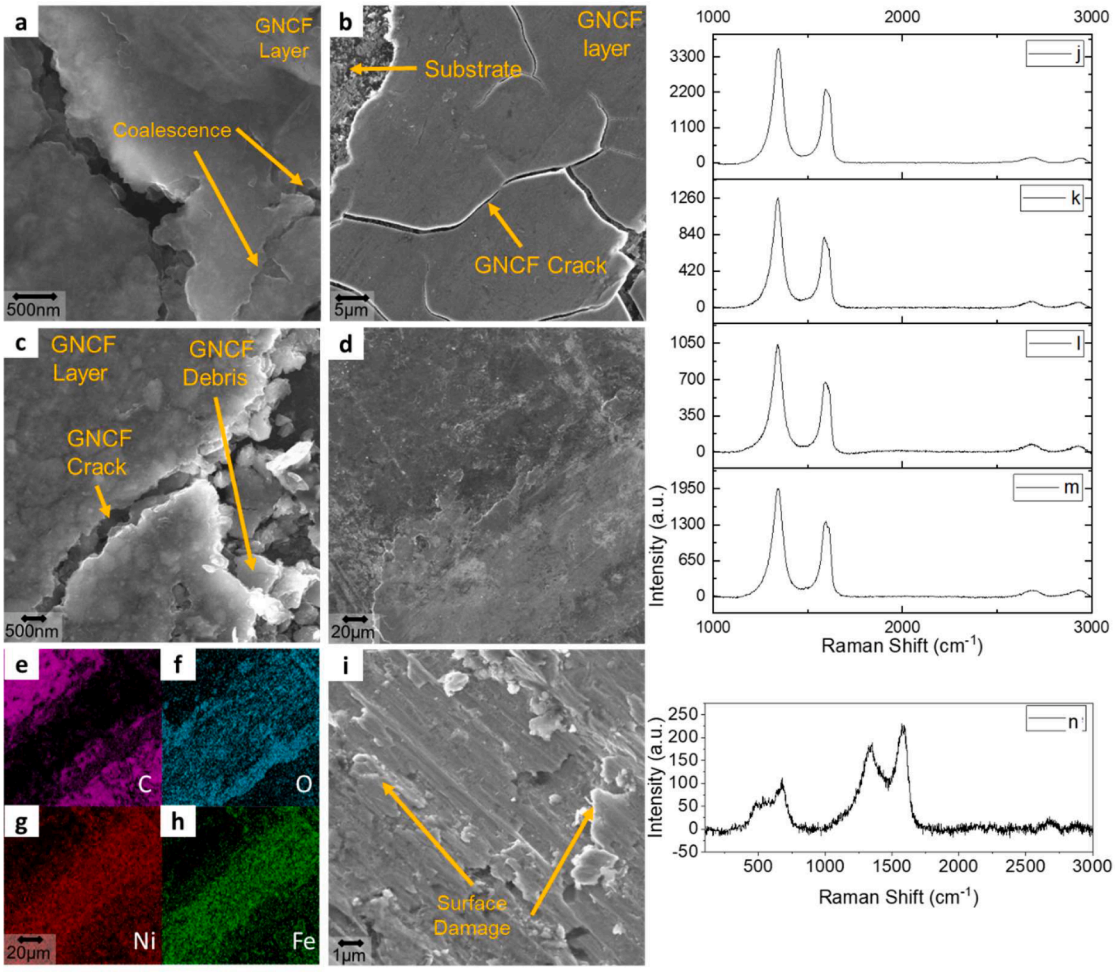

Fig. 13. (a)-(d), SEM images of graphene nanocomposite film on 30 min wear track of Ni-Invar; (e)-(h), EDS results of 30 min wear track of treated Ni Invar, indicating the presence of Fe, C, O and Ni respectively in the wear tracks; (I), SEM image of wear track in the untreated Ni-Invar substrate, after 30 mins of wear (J)-(m), Raman spectra of the composite film in the wear track, indicating the presence of graphene nanocrystals; (n), Raman spectra of 30 min wear track of untreated Ni-Invar showing Nickel oxide peaks.

are carbon nanocrystals that have not been smoothen and serve as carbon nano rollers contributing to reduced coefficients of friction. The sustained number of cycles to failure were ~120,000 for Ni – Invar and ~100,000 for steels. Although, Ti had the lowest number of cycles to failure of ~18,000, it is ~70 % higher than what has been reported [17, 53]. The reduction in CoF and number of cycles to failure values with our method are significant improvements and novel contributions to understanding mechanisms associated with graphene and carbon-based coatings on various metallic substrates.

The microstructural characterization of the wear tracks (Figs. 13 −16) and different variants of carbon signatures were resolved by Raman Spectroscopy. The Raman spectroscopy as shown in Fig 15 (j, k, l, m) confirmed the different carbon variants in the wear tracks. From the spectra, $I_{D/G}$ ratio of 1.04 for graphene oxide, 0.95 for defective or doped multiwalled graphene, and 0.99 for carbon nano tubes/fullerenes were observed. These different carbon signatures based on the $I_{D/G}$ ratios are consistent with published literature [17,47,49,56,57]. The differences in the peak height and morphology of these carbon variants provide the condition for micro contacts points needed to induce superlubricious behaviour on the carbon coated metallic surfaces.

Molecular dynamic simulations were used to provide insights into the mechanisms of the different carbon signatures on superlubricity. This was to ascertain the superlubricious interactions between the substrates and the counter body. The schematic of the ball on disk setup for MD simulation is given in Fig 11(a). The simulations show variations in the friction coefficients as the graphitic ball surface slides over different graphene variants on a graphene substrate (Fig. 11(c). The mean CoF values obtained from the simulations were 0.02, 0.11, 0.003, 0.007, and 0.01, for the sliding of pure graphene, graphene oxide, carbon nanotubes (CNT), fullerene and raptured graphene interactions, respectively. These simulations provide insights into the possible superlubricious nano- and microcontact interactions expected under the ball. The mechanisms observed in the simulations confirmed the reduction of the CoF values by unsmoothed carbon nanotubes and fullerenes, which serve as nano rollers in the contacting surfaces. The superlubricity of the graphitic surfaces is also attributed to atomistic configurations in the carbon nanocrystals' sp^2 / sp^3 carbon shells. These hinder the possibility of atomistic locking in this mechanism [17]. Thus, the interacting layers do not have an energetically desired position with respect to each other. Hence, they slide past each other with negligible energy loss [58]. Thus, the energy barrier to lateral motion is almost eliminated.

The friction coefficient with the coating life achieved in the stabilized regime for the metallic substrates is given in Fig. 11(b). The coating life was estimated as the number of cycles in which the low CoF values ($\leq$ 0.2) were sustained before transitioning to values comparable to those of the untreated substrates. The Ni-Invar had the broadest range of coating lives within the current tested range of carbon-based coatings. The 1045 steel followed this, and then the Ti alloys (which had low cycles to failure with high CoF values in the stabilized regime).

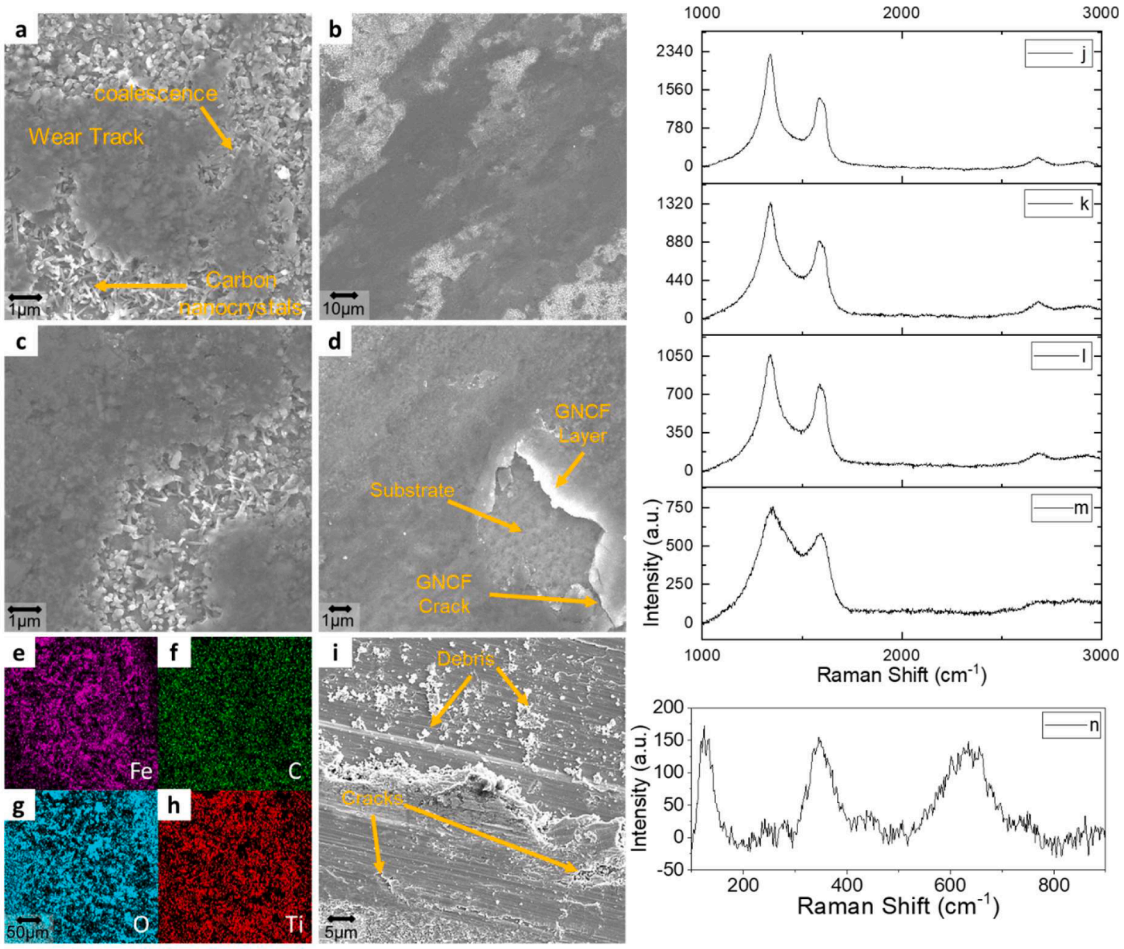

Fig. 14. (a)-(d): SEM images of graphene nanocomposite film on 3 min wear track of CP-Ti, (I – h): EDS results of 3 min wear track of CP-Ti, indicating the presence of Fe, C, O and Ti in the wear tracks, (i): SEM image of 30 min wear track of untreated CP-Ti showing abrasive and adhesion wear, (j – m): Raman spectra of the composite film in the wear track, showing graphene nanocrystals and multiwalled nanotubes; and (n): Raman spectra of 30 min wear track of untreated CP-Ti with titanium oxide peaks.

The significant reduction of CoF values and the more extended number of cycles to failure in the stabilized regime were associated with the surfaces in which the Raman footprints reveal the presence of multilayered and defective graphene footprint, which were on the Ni-Invar and 1045 Steel substrates. It is also important to note that Raman signatures for multiwalled carbon nanotubes/crystals were observed on CP Ti and Ti-6Al-4V substrates after the deposition of carbon (Fig. 7 and Fig. 8). These had high CoF values and shorter numbers of cycles to failure in the stabilized regimes. The superlubricity conditions were identified for loads 2 N and below, at 1000 rpm on substrates that were treated for at least five hours at 900 °C (Fig. 12). Relatively high CoFs have been associated with tests done from 100 - 500 rpm [59, 60]. In this work it was observed that at low velocities (100–500 rpm) the GNCFs delaminated quickly, and this leads to increase CoF values, while at a higher velocity (1000 rpm) the GNCF did not delaminate, but remained attached to the substrates, resulting in lower CoF values. Prior work [59,60] has also shown the dominance of graphene film delamination at relatively low sliding speeds [58,59].

In Fig. 12(a), the angular velocity for the wear test was varied between 100 and 1000 rpm, with corresponding wear track radii adjustments from 3 – 5 mm. These variations resulted in linear velocities ranging from 0.0314 m/s to 0.5236 m/s. These velocities are applicable to diverse applications, spanning from automotive to aerospace industries, reflecting their practical relevance.

The temperatures at the contacting surfaces as measured with the infrared thermometer are 25 ± 0.28 °C for Ni-invar, 24 ± 0.32 °C for steel, 27 ± 0.4 °C for Ti-6Al-4V and 26 ± 0.35 °C for CP – Ti. The observed trends were function of the rate of dissipation of heat into the substrate due to the relative motion between the substrate and the counter body (100Cr balls). The measured temperatures are affected by dynamic heat loss effects during relative sliding of the surfaces in contact. The finite element simulations estimated the temperature at the contacting surface to be about 25 ± 1 °C, which is consistent with the experimental results (Fig. 12(c)).

The above results are consistent with observations of phenomena that are associated with sliding contact of carbon-based materials [18]. Since carbon undergoes tribological oxidation and transformation of graphene structures at the mating surfaces during contact interactions [50], this leads to a drastic reduction in CoFs and wear rates of the carbon-coated metallic substrates (Figs. 11, 13-16).

3.3. *Wear of carbon nanocrystal coating on metallic substrates*

The wear experiments on the carbon-coated and uncoated metallic surfaces revealed different wear rates and coating life. These wear behaviour and coating lives are dependent on the deformation, cracking, and removal of the graphene nanocomposite films (GNCFs) (Fig. 13-17). The GNCFs were formed and sustained in the wear tracks for different cycles to failure and time durations. The extent of the carbon coating and associated protection controlled the mechanisms of wear on the treated substrates.

The SEM images of the wear tracks on the Ni-Invar in Fig. 13 (a-d) (as

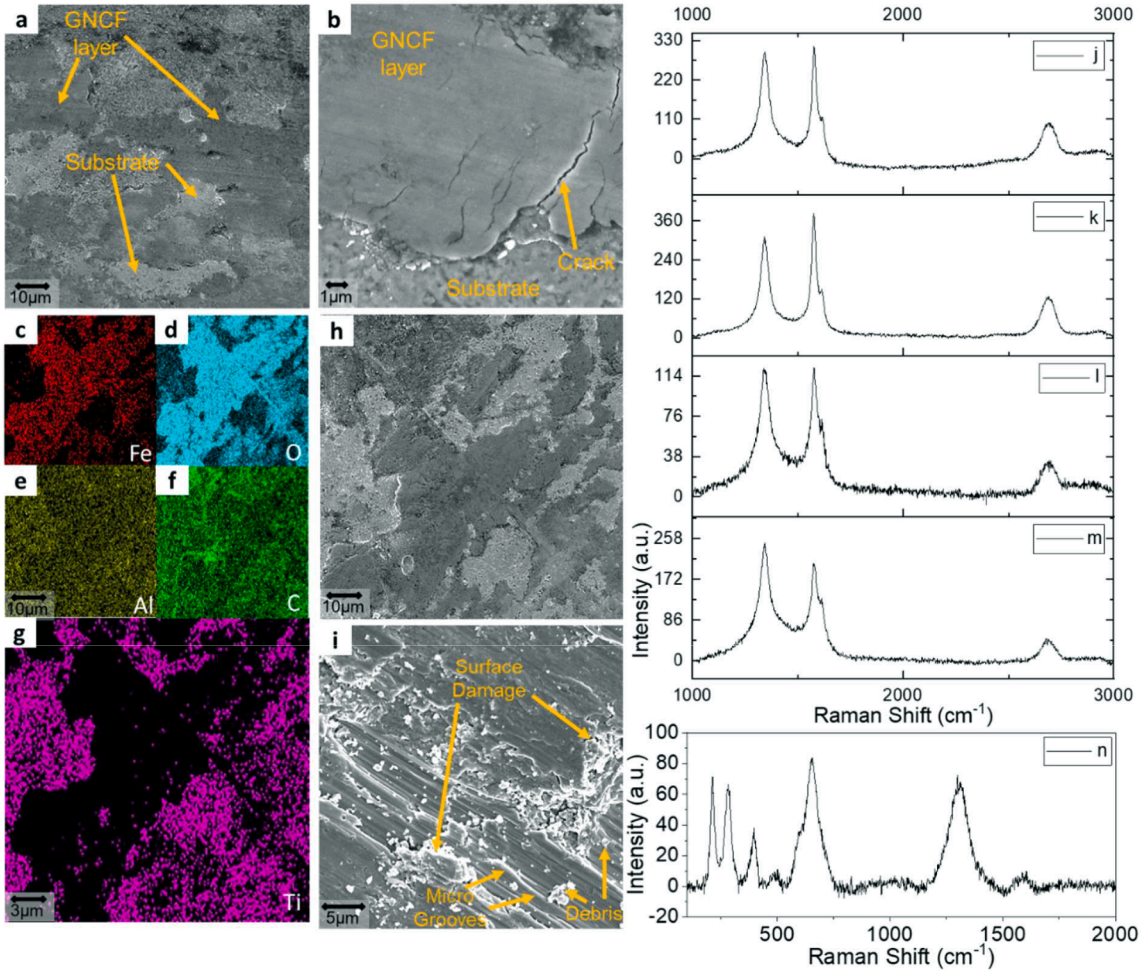

Fig. 15. (a)-(b), SEM images of graphene nanocomposite film on 11 min wear track of Ti-6Al-4V; (c)-(g), EDS results of 11 min wear track of Ti-6Al-4V, indicating the presence of Ti, O, C, Fe and Al respectively in the wear tracks, (h) SEM images of graphene nanocomposite film on 11 min wear track of Ti-6Al-4V, (i) SEM image of 30 min wear track of Ti-6Al-4V showing adhesion and abrasive wear mechanisms and (j)-(m) Raman spectra of the graphitic film in the wear track, indicating the presence of graphene nanocrystals and doped graphene crystals and (n), Raman spectra of 30 min wear track of Ti-6Al-4V showing Titanium oxide peaks.

characterised from three minutes to two hours during wear) reveal the presence of the graphene nanocomposite film in the wear tracks. The film forms under the dynamic contact conditions associated with the sliding of the treated ball on the carbon nanocrystals in the coating, while the GNCF forms on both the ball's surface and the substrate. Cracks and wear debris of the GNCF are observed in the wear tracks, as the number of cycles increases. The GNCF was removed from the wear tracks after ~150,000 cycles of the experiment with a 2 N load. The wear rate of the coated structure was also reduced by ~86 % as compared to the untreated substrates. The EDS analyses (Fig. 13 (e-h)) show substrate elements such as Ni and Fe mixed into the GNCF. The EDS also detected oxygen combining with carbon and the substrate elements to form tribological oxidated products.

The Raman spectra of the GNCF had D at 1346 cm^{-1}, G at 1597 cm^{-1} and 2D bands at 2700 cm^{-1} (Fig. 13 (j-m). The intensity ratio $I_{D/G}$ was 1.27, whereas that of $I_{2D/G}$ was 0.5. This Raman signature is synonymous with graphene nanocrystal films from chemical exfoliation [51, 61] and those on wear tracks of diamond-like carbon surfaces [17]. The graphene nanocrystal films were dominant in the Raman scatter results. However, there were distortions in the initial Raman peaks for the carbon coating on the substrates. This confirms the occurrence of tribologically induced graphitization. The graphitization of the coating layers occurs due to high stresses and temperatures under the counter body, distorting the carbon structure [51,62].

Fig. 13(i) presents an SEM image of a wear track in the untreated Ni-Invar substrate, after 30 min of wear with an untreated 100Cr steel ball. Abrasive wear with surface damage dominates the wear tracks with traces of adhesion wear leading to higher wear rates in the untreated material than in treated ones. No evidence of these two mechanisms was observed on the surfaces of the treated substrates, when the GNCF covered most of the wear tracks, thus prolonging the wear live/cycles to failure. The Raman spectra of the debris on the wear tracks on the untreated material (Fig. 13(n)) revealed the presence of NiO and Fe_2O_3 peaks, which resulted from the adhesion wear interactions of tribological oxidation products.

The SEM images of the wear tracks of the treated 100Cr steel ball on treated CP Ti substrates is given in Fig. 14 (a-d). These images show the early stages of graphene nanocomposite film formation. The multi-walled carbon nanotubes deform, flatten and merge to form the GNCFs under tribological conditions. Preventing the direct contact of the ball material with the substrate material. Thus, the adhesion and abrasive wear mechanisms (Fig. 14(i)) observed on the untreated ball and substrate wear were prevented at this stage of the wear process. The SEM images confirm that the GNCF is removed from the wear tracks after ~18,000 cycles of the wear experiment, showing the end of graphitic protection. Subsequently, abrasive wear, with traces of adhesion wear mechanism dominates the wear. The EDS results also show that Ti and Fe from the substrate and ball materials form part of the bulk chemistry of the GNCF. The results also reveal carbon from the graphitic coating and oxygen from tribological oxidation (Fig. 14 (e-h)).

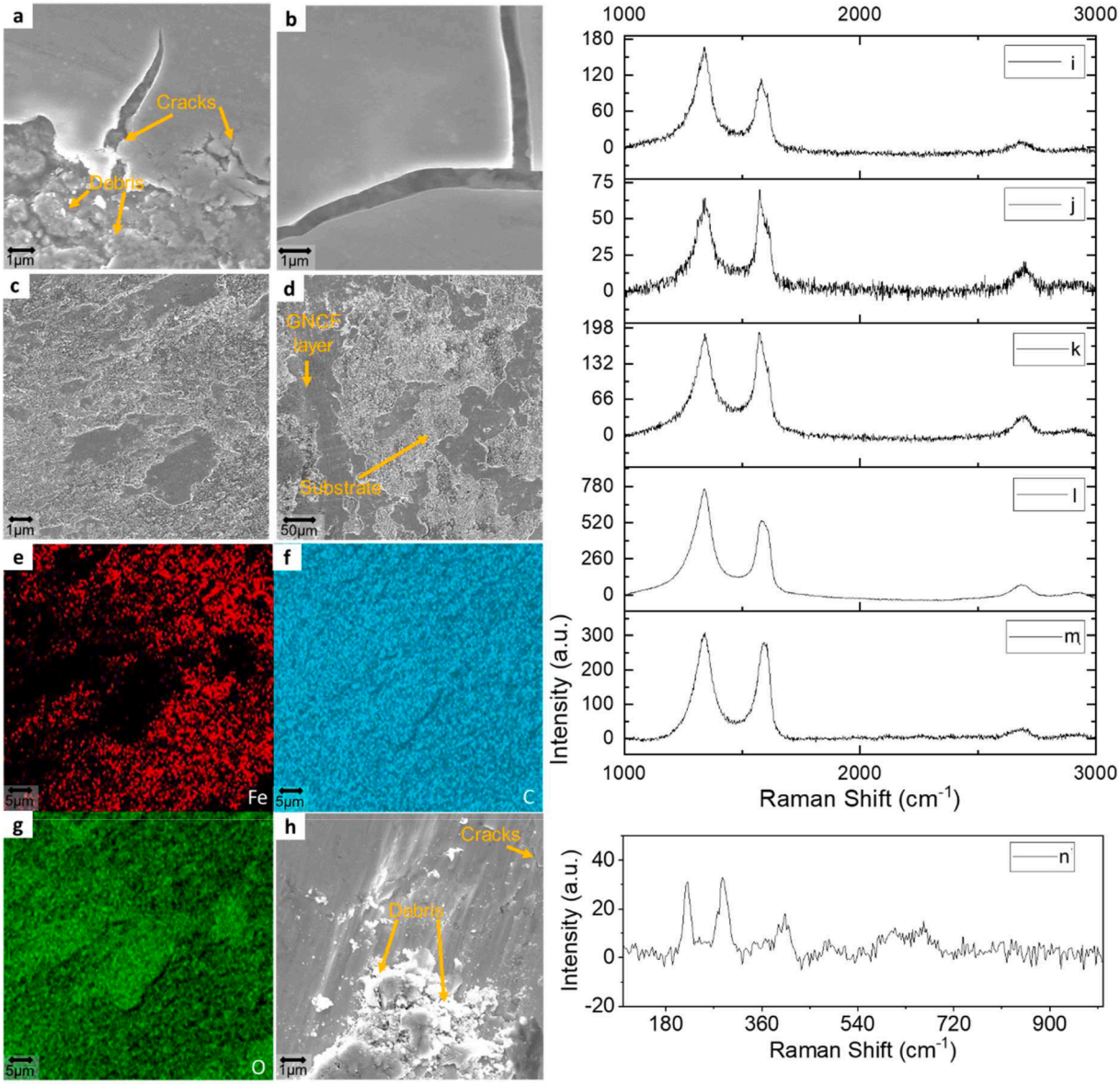

Fig. 16. (a)-(b), SEM images of graphene nanocomposite film on 30 min wear track of 1045 steel; c-d, SEM images of graphene nanocomposite film on 1 h 30 min wear track of 1045 steel; e-g, EDS results of 1 h 30 min wear track of 1045 steel, indicating the presence of C, O and Fe respectively in the wear tracks, h, SEM image of 30 min wear track of untreated 1045 Steel showing adhesion wear mechanisms, i-m, Raman spectra of the composite film in the wear track, indicating the presence of graphene nanocrystals and graphene oxide; and n, Raman spectra of 30 min wear track of untreated 1045 steel showing iron oxide peaks.

The Raman spectra of the wear tracks also showed the distortion of the original carbon footprint on the CP Ti substrate. The spectra revealed the presence of graphene nanocrystals with D, G and 2D bands at 1346 cm^{-1}, 1592 cm^{-1}, and 2694 cm^{-1}, respectively (Fig. 14 (j – m). Carbon signatures, identical to those of the multiwalled carbon nanotubes in the original graphitic coating, were also detected in the wear tracks. Raman spectra for the wear tracks of the untreated substrates show the presence of TiO and Fe_2O_3 debris from the adhesion wear and tribological oxidation activities during the wear process (Fig. 14(n)). The wear rate for the treated CP-Ti substrates was reduced by 84 %, when compared to those of the untreated CP-Ti substrates (Fig. 11 e).

The wear tracks on the treated Ti-6Al-4V substrates are shown in the SEM images in Fig. 15 (a, b, h). These revealed the presence of the GNCF in the wear tracks. The graphitic protection lasted for ~20,000 cycles on these tracks, obscuring the direct contact between the ball material and the substrates. The aggressive abrasive wear with surface cracks and micro groves observed on the untreated Ti-6Al-4V wear tracks (as shown in Fig. 15(i) was prevented during the early stages of wear in the treated substrates. Also, the surface damage and micro groves observed on the wear tracks of the untreated substrate were precluded because of graphitic protection. However, the EDS analyses (Fig. 15 (c – g)) of the wear tracks showed segregation of interacting elements in the wear tracks. The Fe from the 100Cr steel ball was detected at the top of the GNCF layer with little interaction with the substrate material. Oxygen was also detected in regions with high Fe concentrations, suggesting the presence of iron oxides in the GNCF layer, which can be attributed to the effects of tribological oxidation during the wear process.

The Raman spectra of the GNCF on the Ti-6Al-4V wear tracks reveal a change in intensity and structure of the carbon signatures, compared to those of the multiwalled carbon nanotubes detected before the wear tests. The D, G, and 2D peaks were located at 1346 cm^{-1}, 1578 cm^{-1}, and 2694 cm^{-1}, respectively (Fig. 15 (j-m). Three $I_{D/G}$ intensity ratios which are 1.04, 0.95, and 0.99, were detected in the Raman signatures. These ratios indicate the presence of Ti-doped graphene, graphene

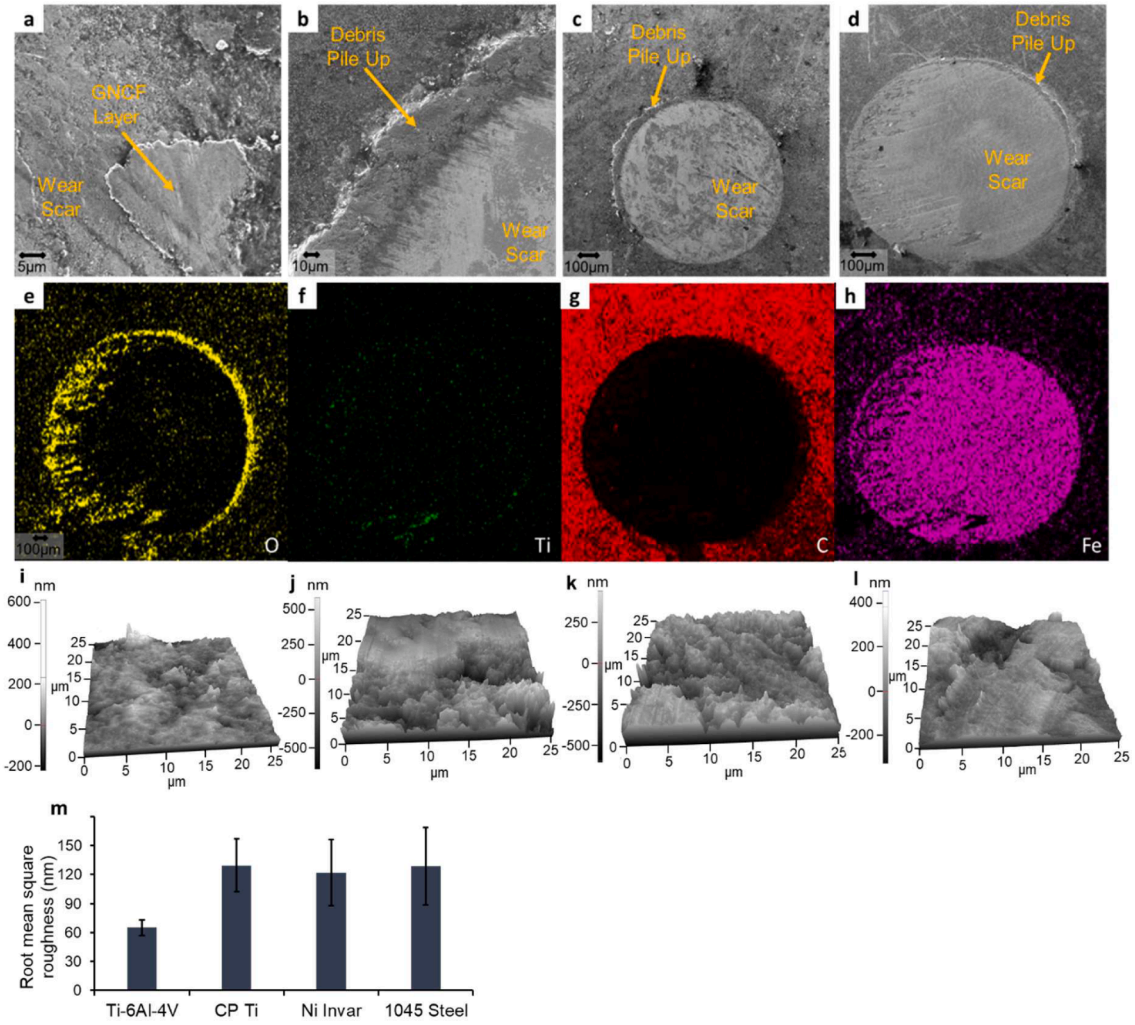

Fig. 17. SEM images of the treated ball for (a) graphene nanocomposite film in ball wear scar for Ni, (b) wear debris pile-up on the ball, (c) 40 mins wear scar on Ti-6Al-4V, (d) 40 min wear scar on CP-Ti; (e-h) EDS results of 40 min wear scar of ball used on treated CP-Ti, indicating the presence of O, Fe, and Ti, respectively, in the wear scar with surrounding deposited carbon. (i)-(l) AFM results of multiple nano- and micro-contact points on the 1000 cycles wear tracks of Ti-6Al-4V, 1045 Steel, CP Ti and Ni-Invar, respectively, (m) Root mean square roughness analysis of the wear tracks of the treated substrates.

nanocrystals, and graphene oxide structures in the graphitic film on the wear tracks. The Raman spectra of the wear debris on the untreated substrates show TiO and Fe_2O_3 peaks in the results (Fig. 15(n)). This relates to adhesion wear interactions from the tribological oxidation of the ball material and the substrate.

The SEM images of the wear tracks of the treated 1045 steel substrate at different time intervals are given in Fig. 16 (a – d). The wear tracks were protected by the GNCFs, which were fully developed in the wear tracks taken ~30 min after the commencement of the wear experiment (Fig. 16 (a-b)). This film prevented the direct contact of the 100Cr ball with the substrate. The SEM images in Fig. 16 (c – d) taken at ~ 90 min after the start of the test, showed depletion of the GNCF on the wear tracks due to the impact of the wear action of the counter body. The wear mechanisms of the untreated 1045 steel substrate are dominated by the adhesion and abrasive (Fig. 16(m)). The EDS analyses (Fig. 16 (e – g)) of the wear tracks showed high concentrations of Fe and O on the graphitic layers, indicating the presence of iron oxide in the graphitic layers.

The Raman spectra for the wear tracks show the presence of graphene oxide with D bands at 1341 cm^{-1}, G bands at 1601 cm^{-1} and 2D bands at 2722 cm^{-1} as shown in Fig. 16 (l – m). The corresponding intensity ratio $I_{D/G}$ was 1.02 and that of the $I_{2D/G}$ was 0.87. The Raman spectra (Fig. 16(n)) for the wear tracks of the untreated surfaces indicate the presence of Fe_2O_3 in the wear debris. The wear rate of the treated substrates was reduced by 77 % compared to the untreated substrates (Fig. 11 e).

The wear scars on of the treated balls used for the wear tests showing the GNCF with the graphitic protection are shown in Fig. 17. The wear debris piled up at the edges of the scar. The EDS analyses of the wear scars (Fig. 17 e – h) showed oxides which is characteristic of high amounts of O, Fe and C in the wear debris. The presence of iron oxide and graphene oxides in the wear debris are products of tribo-oxidation films. There were traces of the substrate elements in the wear scars as shown by the EDS analyses. The wear rates of the counter body (balls) used against the various substrates reduced by 80 % for CP Ti, 84 % for Ti-6Al-4V, 85 % for Ni Invar and 91 % for 1045 steel substrates (Fig. 11 d).

3.4. XRD of coated and uncoated surface of substrates

The X-ray diffraction analyses of the substrates and carbon-coated surfaces are given in Fig. 18. Generally, the coated metallic substrates showed identifiable peaks corresponding to various carbon structures, confirming the results from the Raman spectroscopy. For the iron substrate, the carbon diffusion resulted in phases resolved as BCC iron and iron carbides for test done at 500 °C. At elevated temperatures of 900 °C,

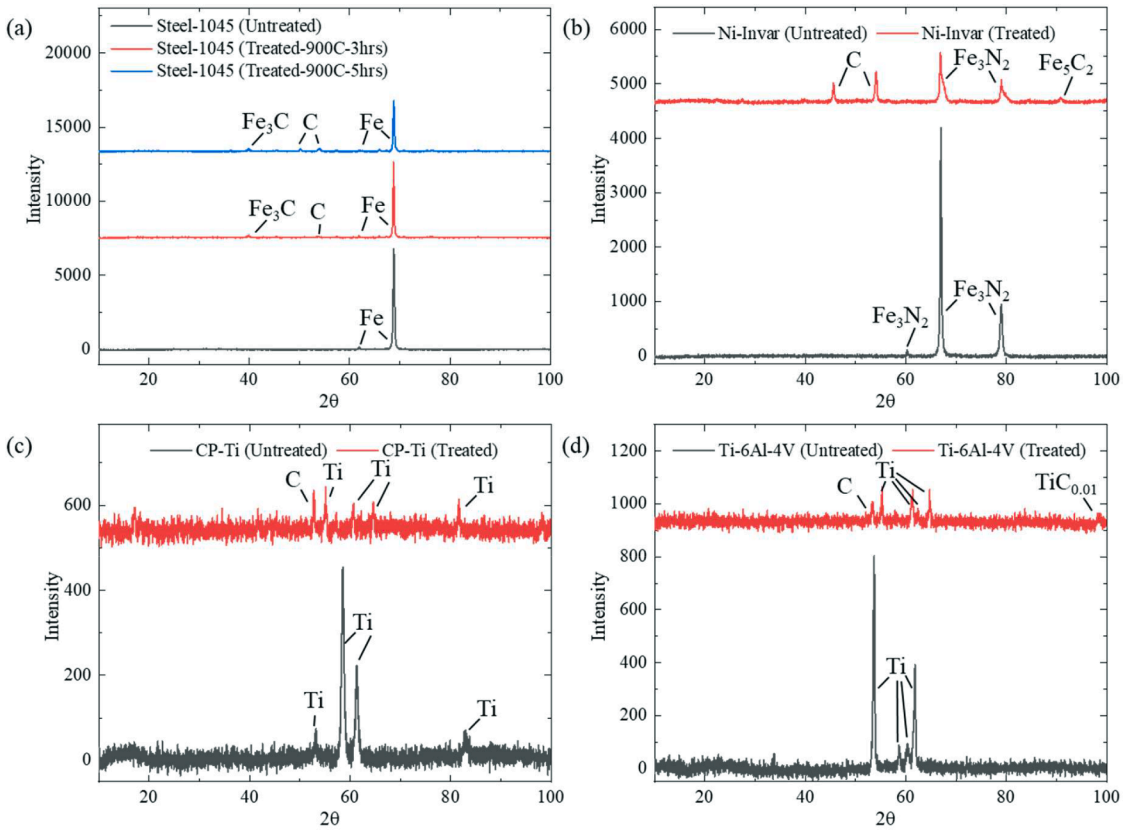

Fig. 18. Comparative XRD patterns of metallic substrates with and without coatings. Displayed are the patterns for commercially pure titanium, Ti-6Al-4V, Ni-invar and 1045 steel. For the case of 1045 steel, the patterns are provided under various coating conditions, illustrating the characteristics and stages of the coating deposition process.

discernible and distinct carbon structures are observed on the surface, which is a function of the processing time and temperature. Similar distinct variants of carbon structures were observed for Ni-Invar and Ti-6Al-4V substrates. Some intermediate phases such as Fe_5C_2 and TiC0.01 were identified and resolved.

Notably, Invar predominantly forms iron-based intermediate structures, whereas commercially pure titanium substrates do not show, displaying only the formation of carbon on the surface. For the parent phases, there was no shift in peaks or peak broadening showing no phase transformation between treated and untreated substrates. Although the XRD analyses were done to resolve the dominant parent phases and some variants of carbon-like phases, it is not the accurate approach to resolve carbon features due to the low electron density of carbon, broadening of peaks associated with carbon and overlapping of peaks. Hence XRD data is more qualitative and complimentary to the Raman spectroscopy, which is a more accurate technique for studying carbon-based materials as used extensively in this study.

4. Conclusion

In conclusion, we introduce a simple method of macroscale metallic superlubricity:

- Carbon nanocrystals with graphene signatures have been deposited using a novel, simple, low-cost, high temperature biowaste treatment method with Manihot esculenta as the carbon source.
- Macroscale superlubricity was attained with coefficients of friction of ~0.003 and was sustained for more than 150,000 cycles before failure at a humidity of 58%. This sets a new milestone for graphitic coatings for wear and friction applications.
- The primary mechanism for the superlubricious behaviour is the many microcontacts points inducing ultralow friction behaviour. This is shown by the atomic force microscopy of the coated metallic surfaces.
- The friction and wear of the treated substrates reveal a corrugated flattening graphene nanocomposite films in the wear tracks, which led to the observed macroscale superlubricity and a reduction and improved wear properties of the carbon-coated Ni-Invar, 1045 steel, CP Ti, and Ti-6Al-4V alloys.
- The coating life index of the carbon-coated metallic materials was determined and established for structural steel, Ni-based alloys, and Ti alloys. This has implication for robust design of next generation carbon-coated materials for various structural and functional applications.

CRediT authorship contribution statement

Tabiri Kwayie Asumadu: Writing – review & editing, Writing – original draft, Methodology, Investigation, Formal analysis, Data curation, Conceptualization. **Mobin Vandadi:** Writing – review & editing, Writing – original draft, Visualization, Validation, Software, Methodology, Investigation, Formal analysis, Data curation. **Desmond Edem Primus Klenam:** Writing – review & editing, Writing – original draft, Methodology, Investigation, Formal analysis, Conceptualization. **Kwadwo Mensah-Darkwa:** Writing – review & editing, Supervision, Conceptualization. **Emmanuel Gikunoo:** Writing – review & editing, Supervision, Project administration, Conceptualization. **Samuel Kwofie:** Writing – review & editing, Supervision, Project administration, Conceptualization. **Nima Rahbar:** Writing – review & editing, Supervision, Software, Resources, Project administration, Conceptualization. **Winston Oluwole Soboyejo:** Writing – review & editing, Supervision,

Resources, Project administration, Funding acquisition, Conceptualization.

Declaration of competing interest

The authors declare that they have no known competing financial interests or personal relationships that could have appeared to influence the work reported in this paper.

Acknowledgment

This work is dedicated to the life and work of the late Prof. Olusegun Oyeleke Adewoye, who was instrumental in the initial work of using Manihot esculenta for strengthening metallic surfaces. Funding from the WPI Global Fund and SUNY Polytechnic Research Foundation are duly acknowledged.

References

[1] K. Holmberg, A. Erdemir, Global impact of friction on energy consumption, economy and environment, FME Trans. 43 (2015) 181–185, https://doi.org/10.5937/fmet1503181H.
[2] J.R. Davis, Surface engineering for corrosion and wear resistance, ASM Int. (2001). ISBN 0-87170-700-4OCLC 1027005806.
[3] O. Hod, E. Meyer, Q. Zheng, M. Urbakh, Structural superlubricity and ultralow friction across the length scales, Nature 563 (2018) 485–492, https://doi.org/10.1038/s41586-018-0704-z.
[4] M. Peyrardi, S. Aubryi, Critical behaviour at the transition by breaking of analyticity in the discrete Frenkel-Kontorova model, J. Phys. C: Solid State Phys. 16 (9) (1983) 1593, https://doi.org/10.1088/0022-3719/16/9/005.
[5] M. Hirano, K. Shinjo, Atomistic locking and friction, Phys. Rev. B 41 (1990) 11837–11851, https://doi.org/10.1103/PhysRevB.41.11837.
[6] M. Dienwiebel, G.S. Verhoeven, N. Pradeep, J.W.M. Frenken, J.A. Heimberg, H. W. Zandbergen, Superlubricity of graphite, Phys. Rev. Lett. 92 (12) (2004) 126101, https://doi.org/10.1103/PhysRevLett.92.126101.
[7] Z. Liu, J. Yang, F. Grey, J.Z. Liu, Y. Liu, Y. Wang, Y. Yang, Y. Cheng, Q. Zheng, Observation of microscale superlubricity in graphite, Phys. Rev. Lett. 108 (20) (2012) 205503, https://doi.org/10.1103/PhysRevLett.108.205503.
[8] A. Ayyagari, K.I. Alam, D. Berman, A. Erdemir, Progress in Superlubricity across different media and material systems — a review, Front. Mech. Eng. 8 (2022) 908497, https://doi.org/10.3389/fmech.2022.908497.
[9] R.C. Sinclair, J.L. Suter, P.V. Coveney, Graphene–graphene interactions: friction, Superlubricity, and exfoliation, Adv. Mater. 30 (2018) 1705791, https://doi.org/10.1002/adma.201705791.
[10] X. Ge, Z. Chai, Q. Shi, Y. Liu, W. Wang, Graphene superlubricity: a review, Friction 11 (11) (2023) 1953–1973, https://doi.org/10.1007/s40544-022-0681-y.
[11] M. Hirano, Superlubricity: a state of vanishing friction, Wear. 254 (2003) 932–940, https://doi.org/10.1016/S0043-1648(03)00295-3.
[12] J.M. Martin, Superlubricity of molybdenum disulfide. Superlubricity, Elsevier B.V., 2007, pp. 207–225, https://doi.org/10.1016/B978-044452772-1/50044-5.
[13] M. Urbakh, Towards macroscale superlubricity, Nat. Nanotechnol. 8 (2013) 893–894, https://doi.org/10.1038/nnano.2013.244.
[14] X. Chen, J. Li, Superlubricity of carbon nanostructures, Carbon 158 (2020) 1–23, https://doi.org/10.1016/j.carbon.2019.11.077.
[15] M.Z. Baykara, M.R. Vazirisereshk, A. Martini, Emerging superlubricity: a review of the state of the art and perspective on future research, Appl. Phys. Rev. 5 (2018), 041102_1-041102_20.
[16] P. Ball, A new twist on superlubricity, Nat. Mater. 18 (2019) 773–774, https://doi.org/10.1038/s41563-019-0383-7.
[17] D. Berman, S.A. Deshmukh, S.K.R.S. Sankaranarayanan, A. Erdemir, A.V. Sumant, Macroscale superlubricity enabled by graphene nanoscroll formation, Science. 348 (6239) (2015) 1118–1122, https://doi.org/10.1126/science.1262024.
[18] D. Berman, A. Erdemir, A.V. Sumant, Graphene: a new emerging lubricant, Materials Today 17 (2014) 31–42, https://doi.org/10.1016/j.mattod.2013.12.003.
[19] W. Song, J. Li, C. Zeng, C. Ouyang, S. Sun, K. Wang, J. Li, J. Luo, Tribo-catalysis triggered the in-situ formation of amphiphilic molecules to reduce friction and wear, Tribol. Int. 185 (2023) 108541, https://doi.org/10.1016/j.triboint.2023.108541.
[20] M. Hirano, K. Shinjo, R. Kaneko, Y. Murata, Anisotropy of frictional forces in muscovite mica, Phys. Rev. Lett. 67 (1991) 2642–2645, https://doi.org/10.1103/PhysRevLett.67.2642.
[21] Y. Li, N. Hu, G. Yamamoto, Z. Wang, T. Hashida, H. Asanuma, C. Dong, T. Okabe, M. Arai, H. Fukunaga, Molecular mechanics simulation of the sliding behavior between nested walls in a multi-walled carbon nanotube, Carbon 48 (2010) 2934–2940, https://doi.org/10.1016/j.carbon.2010.04.031.
[22] J. Sun, Y. Zhang, Z. Lu, Q. Li, Q. Xue, S. Du, J. Pu, L. Wang, Superlubricity enabled by pressure-induced friction collapse, J. Phys. Chem. Lett. 9 (2018) 2554–2559, https://doi.org/10.1021/acs.jpclett.8b00877.
[23] M. Yamamoto, M. Stopa, Y. Tokura, Y. Hirayama, S. Tarucha, Negative Coulomb drag in a one-dimensional wire, Science. 313 (5784) (2006) 204–207, https://doi.org/10.1126/science.1126601.
[24] E. Thormann, Negative friction coefficients, Nat. Mater. 12 (6) (2013) 468, https://doi.org/10.1038/nmat3656.
[25] J.M. Martin, C. Donnet, Th. Le Mogne, Th. Epicier, Superlubricity of molybdenum disulphide, Phys. Rev. B 48 (1993) 10583–10586, https://doi.org/10.1103/PhysRevB.48.10583.
[26] D. Berman, S.A. Deshmukh, S.K.R.S. Sankaranarayanan, A. Erdemir, A.V. Sumant, Macroscale superlubricity enabled by graphene nanoscroll formation, Science 348 (6239) (2015) 1115–1118, https://doi.org/10.1126/science.1261422.
[27] P. Li, P. Ju, L. Ji, H. Li, X. Liu, L. Chen, H. Zhou, J. Chen, Toward robust macroscale superlubricity on engineering steel substrate, Adv. Mater. 32 (36) (2020) 2002039, https://doi.org/10.1002/adma.202002039.
[28] X. Ge, Z. Chai, Q. Shi, J. Li, J. Tang, Y. Liu, W. Wang, Functionalized graphene-oxide nanosheets with amino groups facilitate macroscale superlubricity, Friction 11 (2) (2023) 187–200, https://doi.org/10.1007/s40544-021-0583-4.
[29] C. Androulidakis, E.N. Koukaras, G. Paterakis, G. Trakakis, C. Galiotis, Tunable macroscale structural superlubricity in two-layer graphene via strain engineering, Nat. Commun. 11 (1) (2020) 1595, https://doi.org/10.1038/s41467-020-15446-y.
[30] Y. Song, C. Qu, M. Ma, Q. Zheng, Structural superlubricity based on crystalline materials, Small 16 (2020) 1903018, https://doi.org/10.1002/smll.201903018.
[31] S.S. Perry, W.T. Tysoe, Frontiers of fundamental tribological research, Tribol. Lett. 19 (2005) 151–161, https://doi.org/10.1007/s11249-005-6142-8.
[32] A.P. Thompson, H.M. Aktulga, R. Berger, D.S. Bolintineanu, W.M. Brown, P. S. Crozier, P.J. in 't Veld, A. Kohlmeyer, S.G. Moore, T.D. Nguyen, R. Shan, M. J. Stevens, J. Tranchida, C. Trott, S.J. Plimpton, LAMMPS - a flexible simulation tool for particle-based materials modeling at the atomic, meso, and continuum scales, Comput. Phys. Commun. 271 (2022) 108171, https://doi.org/10.1016/j.cpc.2021.108171.
[33] A. Stukowski, Visualization and analysis of atomistic simulation data with OVITO–the Open visualization tool, Model. Simul. Mat. Sci. Eng. 18 (2010) 015012, https://doi.org/10.1088/0965-0393/18/1/015012.
[34] S.J. Stuart, A.B. Tutein, J.A. Harrison, A reactive potential for hydrocarbons with intermolecular interactions, J. Chem. Phys. 112 (2000) 6472–6486, https://doi.org/10.1063/1.481208.
[35] T. Werder, J.H. Walther, R.L. Jaffe, T. Halicioglu, P. Koumoutsakos, On the Water−Carbon interaction for use in molecular dynamics simulations of graphite and carbon nanotubes, J. Phys. Chem. B 107 (2003) 1345–1352, https://doi.org/10.1021/jp0268112.
[36] H. Ding, Y.C. Shin, A metallo-thermomechanically coupled analysis of orthogonal cutting of AISI 1045 steel, J. Manuf. Sci. Eng. 134 (2012) 051014-1–051014-12, https://doi.org/10.1115/1.4007464.
[37] X. Li, W. Cai, L. Colombo, R.S. Ruoff, Evolution of graphene growth on Ni and Cu by carbon isotope labeling, Nano Lett. 9 (2009) 4268–4272, https://doi.org/10.1021/nl902515k.
[38] T.K. Asumadu, K. Mensah-Darkwa, E. Gikunoo, D.E.P. Klenam, M. Vandadi, N. Rahbar, S. Kwofie, W.O. Soboyejo, Strain gradient plasticity phenomenon in surface treated plain carbon steel, Mater. Sci. Eng.: A 871 (2023) 144806, https://doi.org/10.1016/j.msea.2023.144806.
[39] D.M. Seo, T.W. Hwang, Y.H. Moon, Carbonitriding of Ti-6Al-4V alloy via laser irradiation of pure graphite powder in nitrogen environment, Surf. Coat. Technol. 363 (2019) 244–254, https://doi.org/10.1016/j.surfcoat.2019.02.038.
[40] Y. Zhang, L. Gomez, F.N. Ishikawa, A. Madaria, K. Ryu, C. Wang, A. Badmaev, C. Zhou, Comparison of graphene growth on single-crystalline and polycrystalline Ni by chemical vapor deposition, J. Phys. Chem. Lett. 1 (2010) 3101–3107, https://doi.org/10.1021/jz1011466.
[41] P.N. Belkin, S.A. Kusmanov, I.G. Dyakov, M.R. Komissarova, V.I. Parfenyuk, Anode plasma electrolytic carburizing of commercial pure titanium, Surf. Coat. Technol. 307 (2016) 1303–1309, https://doi.org/10.1016/j.surfcoat.2016.04.057.
[42] E.K. Arthur, E. Ampaw, M.G.Z. Kana, K.J. Akinluwade, A.R. Adetunji, O. O. Adewoye, W.O. Soboyejo, Indentation size effects in pack carbo-nitrided AISI 8620 steels, Mater. Sci. Eng. A 644 (2015) 347–357, https://doi.org/10.1016/j.msea.2015.07.040.
[43] S.M. Zamzamian, S.A. Hossein Feghhi, M. Samadfam, A study on the mobility of edge dislocation in low-carbon α-Fe and its interactions with damage cascade: on picosecond time scale using molecular dynamics simulations, J. Nucl. Mater. 527 (2019) 151806, https://doi.org/10.1016/j.jnucmat.2019.151806.
[44] L. Bokobza, J. Zhang, Raman spectroscopic characterization of multiwall carbon nanotubes and of composites, Express. Polym. Lett. 6 (2012) 601–608, https://doi.org/10.3144/expresspolymlett.2012.63.
[45] A. Reina, X. Jia, J. Ho, D. Nezich, H. Son, V. Bulovic, M.S. Dresselhaus, K. Jing, Large area, few-layer graphene films on arbitrary substrates by chemical vapor deposition, Nano Lett. 9 (2009) 30–35, https://doi.org/10.1021/nl801827v.
[46] A.C. Ferrari, D.M. Basko, Raman spectroscopy as a versatile tool for studying the properties of graphene, Nat. Nanotechnol. 8 (2013) 235–246, https://doi.org/10.1038/nnano.2013.46.
[47] A.C. Ferrari, J.C. Meyer, V. Scardaci, C. Casiraghi, M. Lazzeri, F. Mauri, S. Piscanec, D. Jiang, K.S. Novoselov, S. Roth, A.K. Geim, Raman spectrum of graphene and graphene layers, Phys. Rev. Lett. 97 (18) (2006) 187401, https://doi.org/10.1103/PhysRevLett.97.187401.
[48] A.C. Ferrari, Raman spectroscopy of graphene and graphite: disorder, electron-phonon coupling, doping and nonadiabatic effects, Solid. State Commun. 143 (2007) 47–57, https://doi.org/10.1016/j.ssc.2007.03.052.

[49] A.C. Ferrari, J. Robertson, Interpretation of Raman spectra of disordered and amorphous carbon, Phys. Rev. B. 61 (20) (2000) 14095, https://doi.org/10.1103/PhysRevB.61.14095.
[50] L. Zhang, H. Li, K.-T. Yue, S.-L. Zhang, X. Wu, J. Zi, Z. Shi, Z. Gu, Effects of intense laser irradiation on Raman intensity features of carbon nanotubes, Phys. Rev. B 65 (2002) 073401, https://doi.org/10.1103/PhysRevB.65.073401.
[51] C. Chen, P. Xue, D. Diao, Graphitization vs tribo-oxidation governing friction behaviors of doped graphene nanocrystalline carbon films, Carbon 197 (2022) 435–443, https://doi.org/10.1016/j.carbon.2022.07.001.
[52] Z. Deng, A. Smolyanitsky, Q. Li, X.Q. Feng, R.J. Cannara, Adhesion-dependent negative friction coefficient on chemically modified graphite at the nanoscale, Nat. Mater. 11 (2012) 1032–1037, https://doi.org/10.1038/nmat3452.
[53] P. Wu, X. Li, C. Zhang, X. Chen, S. Lin, H. Sun, C.-T. Lin, H. Zhu, J. Luo, Self-assembled graphene film as low friction solid lubricant in macroscale contact, ACS. Appl. Mater. Interfaces. 9 (2017) 21554–21562, https://doi.org/10.1021/acsami.7b04599.
[54] Y. Song, D. Mandelli, O. Hod, M. Urbakh, M. Ma, Q. Zheng, Robust microscale superlubricity in graphite/hexagonal boron nitride layered heterojunctions, Nat. Mater. 17 (2018) 894–899, https://doi.org/10.1038/s41563-018-0144-z.
[55] R. Zhang, Z. Ning, Y. Zhang, Q. Zheng, Q. Chen, H. Xie, Q. Zhang, W. Qian, F. Wei, Superlubricity in centimetres-long double-walled carbon nanotubes under ambient conditions, Nat. Nanotechnol. 8 (2013) 912–916, https://doi.org/10.1038/nnano.2013.217.
[56] G.J.H. Melvin, Q.-Q. Ni, Y. Suzuki, T. Natsuki, Microwave-absorbing properties of silver nanoparticle/carbon nanotube hybrid nanocomposites, J. Mater. Sci. 49 (2014) 5199–5207, https://doi.org/10.1007/s10853-014-8229-9.
[57] F.T. Johra, J.-W. Lee, W.-G. Jung, Facile and safe graphene preparation on solution based platform, J. Ind. Eng. Chem. 20 (2014) 2883–2887, https://doi.org/10.1016/j.jiec.2013.11.022.
[58] C. Qu, S. Shi, M. Ma, Q. Zheng, Rotational instability in Superlubric joints, Phys. Rev. Lett. 122 (24) (2019) 246101, https://doi.org/10.1103/PhysRevLett.122.246101.
[59] F.A. Essa, A.H. Elsheikh, J. Yu, O.A. Elkady, B. Saleh, Studies on the effect of applied load, sliding speed and temperature on the wear behavior of M50 steel reinforced with Al2O3 and /or graphene nanoparticles, J. Mater. Res. Technol. 12 (2021) 283–303, https://doi.org/10.1016/j.jmrt.2021.02.082.
[60] S. Gao, L.H. Yang, Y. Gan, Q. Chen, The influence of sliding speed on the friction behavior of silica surface, ACS. Omega 6 (2021) 3384–3389, https://doi.org/10.1021/acsomega.0c05897.
[61] A. Kaniyoor, S. Ramaprabhu, A Raman spectroscopic investigation of graphite oxide derived graphene, AIP. Adv. 2 (3) (2012) 032183-1–032183-13, https://doi.org/10.1063/1.4756995.
[62] M. Ghazinejad, S. Holmberg, O. Pilloni, L. Oropeza-Ramos, M. Madou, Graphitizing non-graphitizable carbons by stress-induced routes, Sci. Rep. 7 (1) (2017) 16551, https://doi.org/10.1038/s41598-017-16424-z.